HHS Public Access

Author manuscript

Cell Metab. Author manuscript; available in PMC 2021 December 01.

Published in final edited form as:

Cell Metab. 2020 December 01; 32(6): 996–1011.e7. doi:10.1016/j.cmet.2020.10.022.

Protein prenylation drives discrete signaling programs for the differentiation and maintenance of effector T_{reg} cells

Wei Su[1,2], **Nicole M. Chapman**[1], **Jun Wei**[1], **Hu Zeng**[1], **Yogesh Dhungana**[1], **Hao Shi**[1], **Jordy Saravia**[1], **Peipei Zhou**[1], **Lingyun Long**[1], **Sherri Rankin**[1], **KC Anil**[1], **Peter Vogel**[3], **Hongbo Chi**[1,4,*]

[1]Department of Immunology, St. Jude Children's Research Hospital, Memphis, Tennessee 38105, USA.

[2]Integrated Biomedical Science Program, University of Tennessee Health Science Center, Memphis, Tennessee 38103, USA.

[3]Department of Pathology, St. Jude Children's Research Hospital, Memphis, Tennessee 38105, USA.

[4]Lead contact.

Summary

Effector regulatory T (eT_{reg}) cells are essential for immune tolerance and depend upon T cell receptor (TCR) signals for generation. The immunometabolic signaling mechanisms that promote the differentiation and maintenance of eT_{reg} cells remain unclear. Here, we show that isoprenoid-dependent posttranslational lipid modifications dictate eT_{reg}-cell accumulation and function by intersecting with TCR-induced intracellular signaling. We find that isoprenoids are essential for activated T_{reg}-cell suppressive activity, and T_{reg} cell-specific deletion of the respective farnesylation- and geranylgeranylation-promoting enzymes Fntb or Pggt1b leads to the development of fatal autoimmunity, associated with reduced eT_{reg}-cell accumulation. Mechanistically, Fntb promotes eT_{reg}-cell maintenance by regulating mTORC1 activity and ICOS expression. In contrast, Pggt1b acts as a rheostat of TCR-dependent transcriptional programming and Rac-mediated signaling for establishment of eT_{reg}-cell differentiation and immune tolerance. Therefore, our results identify bidirectional metabolic signaling, specifically between

*Correspondence should be addressed to**: Hongbo Chi**, Department of Immunology, St. Jude Children's Research Hospital, Memphis, TN 38105, USA. Phone: 901-595-6282; Fax: 901-595-5766; hongbo.chi@stjude.org.

Author contributions

W.S. designed, performed, and analyzed cellular, molecular and biochemical experiments, and co-wrote the manuscript; N.M.C. performed and analyzed cellular experiments, co-directed the study, and co-wrote the manuscript; J.W. designed and analyzed experiments, edited the manuscript, and co-directed the study; H.Z. designed, performed, and analyzed cellular experiments; N.M.C., J.W. and H.Z. contributed equally to this work; H.S. performed cellular experiments; Y.D. performed bioinformatic analysis; J.S. performed ATAC-Seq analyses; P.Z. and L.L. packaged retrovirus and helped with generation of retrogenic mice; S.R. measured the survival; A.K. did genotyping of newborn mice; P.V. performed histopathology analysis; H.C. designed experiments, co-wrote the manuscript, and provided overall direction.

Declaration of interests

H. Chi is a consultant for Kumquat Biosciences, Inc.

immunoreceptor signaling and metabolism-mediated posttranslational lipid modifications, for the differentiation and maintenance of eT_{reg} cells.

Graphical Abstract

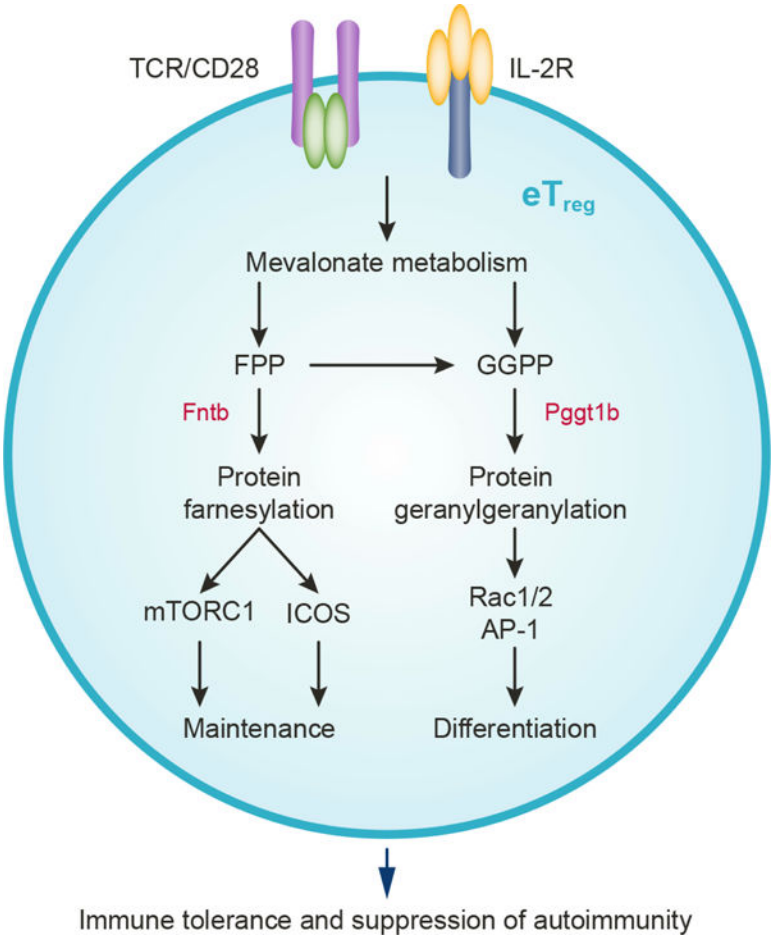

eTOC blurb

Su et al. show that mevalonate metabolism-driven protein geranylgeranylation and farnesylation orchestrate the respective differentiation and maintenance of effector Treg cells, by serving as rheostats for immunological receptor, mTORC1, and Rac signaling. These data establish a crucial role for metabolism-dependent posttranslational lipid modifications in Treg cell-mediated immune suppression.

Introduction

Foxp3-expressing regulatory T (T_{reg}) cells are crucial for establishing self-tolerance, which depends on the conversion of central T_{reg} (cT_{reg}) cells into effector T_{reg} (eT_{reg}) cells during homeostasis and inflammation (Li and Rudensky, 2016; Savage et al., 2020). eT_{reg} cells display superior suppressive activity than cT_{reg} cells and promote tolerance in non-lymphoid tissues (Smigiel et al., 2014; Whibley et al., 2019). eT_{reg}-cell development and function are

programmed by T cell receptor (TCR), co-stimulation and IL-2 signals (Li and Rudensky, 2016). While transcriptional regulators mediate eT_{reg}-cell generation (Cretney et al., 2011; Oh et al., 2017; Vasanthakumar et al., 2017; Vasanthakumar et al., 2015), the metabolic and signaling mechanisms that promote the differentiation and maintenance of eT_{reg} cells remain poorly defined.

Metabolism dictates T_{reg}-cell function and differentiation and is programmed by selective kinase signaling (Galgani et al., 2016; Newton et al., 2016), including PI3K (Huynh et al., 2015; Shrestha et al., 2015) and mTORC1 (Zeng et al., 2013). Emerging studies also show that intracellular metabolites can influence signaling events. For instance, chromatin and DNA modifying enzymes use metabolic intermediates as substrates and cofactors, which can affect Foxp3 expression (Galgani et al., 2016; Newton et al., 2016). Whether intracellular metabolites interplay with cellular signaling to control T_{reg}-cell differentiation or function is underexplored. In response to TCR and IL-2 signals, mTORC1 induces mevalonate metabolism (Zeng et al., 2013), which shapes T_{reg}-cell functional fitness (Lacher et al., 2017; Zeng et al., 2013). Aside from cholesterol, the mevalonate pathway generates the isoprenoids farnesyl pyrophosphate (FPP) and geranylgeranyl pyrophosphate (GGPP) (Wang and Casey, 2016), which mediate posttranslational lipid modifications that are driven by the farnesyltransferase (catalytic subunit encoded by *Fntb*) and geranylgeranyltransferase type 1 (catalytic subunit encoded by *Pggt1b*), respectively. The functions of these metabolism-dependent posttranslational lipid modifications, and whether Fntb and Pggt1b play shared or discrete roles in T_{reg} cells, remain unknown.

Here we show that mevalonate metabolism-dependent posttranslational lipid modifications serve as metabolic rheostats for the temporal fate decisions of eT_{reg} cells. Isoprenoids are crucial for establishing activated T_{reg}-cell suppressive activity, and T_{reg} cell-specific deletion of Fntb or Pggt1b triggers development of a fatal autoimmune disease associated with impaired eT_{reg}-cell accumulation. Mechanistically, Fntb promotes mTORC1 activity and inducible costimulator (ICOS) expression that is crucial for eT_{reg}-cell maintenance, while Pggt1b orchestrates TCR and downstream Rac signaling to promote eT_{reg}-cell differentiation. Thus, our study unveils discrete roles for metabolism-dependent posttranslational lipid modifications and their interplay with immune signaling for balancing the generation and maintenance of eT_{reg} cells to enforce self-tolerance.

Results

Isoprenoids are critical for T_{reg}-cell activation and suppressive function

Metabolism directs T_{reg}-cell function (Galgani et al., 2016; Newton et al., 2016), but the specific metabolic programs that support eT_{reg} cells are unclear. As metabolic pathways upregulated during T_{reg}-cell activation may influence eT_{reg}-cell programming, we performed gene set enrichment analysis (GSEA) of public datasets: 1) activated T_{reg} cells from *Foxp3*^{DTR} mice (DTR, diphtheria toxin receptor) with acute treatment of diphtheria toxin (DT) to induce partial T_{reg}-cell depletion, followed by their activation *in vivo* (Arvey et al., 2014); and 2) T_{reg} cells activated with anti-CD3/28 antibodies for 4 h (Wakamatsu et al., 2013). GSEA showed that hallmark pathways involved in cell proliferation (G2M checkpoint and mitotic spindle) and mTORC1 signaling were enriched upon T_{reg}-cell

activation *in vivo* and *in vitro* [false discovery rate (FDR) < 0.001; Figure 1A]. The cholesterol homeostasis hallmark pathway was the only metabolic program strongly enriched in activated compared with resting T_{reg} cells (Figure 1A), with upregulated expression of multiple genes involved in mediating cholesterol biosynthesis and isoprenoid-dependent posttranslational lipid modifications (Mullen et al., 2016; Wang and Casey, 2016) (Figure 1B and C and Figure S1A). Specifically, *Hmgcr* (3-hydroxy-3-methylglutaryl-CoA reductase), *Hmgcs1* (3-hydroxy-3-methylglutaryl-CoA synthase 1), *Ggps1* (geranylgeranyl diphosphate synthase 1; promotes GGPP synthesis), *Fnta* (common subunit of the prenyl transferases), and *Pggt1b*, but not *Fntb*, showed increased expression upon 4 h of TCR stimulation (Figure 1B and C). Except for *Fntb*, these genes were also upregulated by TCR in naïve and $CD44^{hi}CD62L^{lo}$ effector/memory $CD4^+$ T cells, with less pronounced upregulation of *Hmgcr* and *Hmgcs1* than in T_{reg} cells (Figure S1B). Thus, TCR activation induces gene expression changes in the mevalonate pathway and isoprenoid-dependent protein prenylation.

We next activated T_{reg} cells with TCR in the presence of the Hmgcr inhibitor simvastatin to establish the function of mevalonate intermediates, especially isoprenoids. Simvastatin treatment decreased cell size (FSC-A), increased CD62L expression, and reduced proliferation (indicated by the dilution of Celltrace Violet, CTV) (Figure 1D and E); as expected, mevalonate addition completely restored T_{reg}-cell activation in the presence of simvastatin (Figure 1D and E). Notably, simvastatin-treated T_{reg} cells showed defects in protein prenylation, as indicated by the presence of unprenylated HDJ2 (a farnesylation target) and unprenylated Rap1A (a geranylgeranylation target); prenylation of HDJ2 was rectified by addition of mevalonate or FPP, while Rap1A prenylation was restored by mevalonate or GGPP (Figure S1C). Addition of FPP also rescued the effects of simvastatin treatment on cell size and proliferation, but not CD62L expression, whereas GGPP largely rectified all these parameters (Figure 1D and E). Also, FPP or GGPP partially restored the suppressive function of simvastatin-treated T_{reg} cells (Figure 1F and G), whereas cholesterol supplementation had no effect (Figure S1D). Furthermore, T_{reg}-cell suppressive activity was dampened by DGBP, an inhibitor of Ggps1 (Figure S1A), and this defect was reversed upon addition of GGPP (Figure S1E). Together, these results demonstrate that isoprenoids are essential for T_{reg}-cell activation and suppressive function.

Fntb and Pggt1b in T_{reg} cells are indispensable for immune homeostasis

As isoprenoids mediate protein prenylation (Figure S1A) and the expression of *Fnta* and *Pggt1b* was increased upon T_{reg}-cell activation (Figure 1B and C), we next tested if isoprenoids establish T_{reg}-cell function via posttranslational lipid modifications. We generated mice with T_{reg} cell-specific deletion of *Fntb* or *Pggt1b* by breeding mice with floxed *Fntb* (*Fntb*$^{fl/fl}$) or *Pggt1b* (*Pggt1b*$^{fl/fl}$) alleles (Du et al., 2020; Khan et al., 2011; Liu et al., 2010) with those expressing Foxp3-driven Cre recombinase (*Foxp3*^{Cre}) (Rubtsov et al., 2008). *Fntb* or *Pggt1b* expression was lost in T_{reg} cells, but not conventional T cells, from *Foxp3*^{Cre}*Fntb*$^{fl/fl}$ or *Foxp3*^{Cre}*Pggt1b*$^{fl/fl}$ mice, respectively (Figure S2A and B). These mice also had reduced prenylation of specific substrates of Fntb (HDJ2) and Pggt1b (Rap1A) in T_{reg} cells, but not conventional $CD4^+$ T cells (Figure S2C and D), validating inhibition of protein farnesylation and geranylgeranylation by deletions of Fntb and Pggt1b,

respectively. Further, Fntb- and Pggt1b-deficient T_{reg} cells had impaired suppressive function *in vitro* (Figure S2E and F), revealing important roles for Fntb and Pggt1b for T_{reg}-cell suppressive activity.

Consistent with the effects on T_{reg}-cell suppressive function, we found that Fntb and Pggt1b were crucial for enforcing T_{reg} cell-mediated self-tolerance *in vivo*, as *Foxp3*^{Cre}*Fntb*$^{fl/fl}$ and *Foxp3*^{Cre}*Pggt1b*$^{fl/fl}$ mice developed a *Scurfy*-like autoimmune disease, characterized by runted body size (Figure 2A), systemic inflammation (see below) and rapid death (Figure 2B). An earlier lethality was observed in *Foxp3*^{Cre}*Pggt1b*$^{fl/fl}$ (median survival of 23 days) as compared with *Foxp3*^{Cre}*Fntb*$^{fl/fl}$ mice (median survival of 42 days) (Figure 2B). These mutant mice had increased size and cellularity of the spleen and peripheral lymph nodes (pLN) (Figure 2C). Excessive inflammatory infiltrates were observed in multiple tissues (Figure 2D), including CD4$^+$ and CD8$^+$ T cells, arginase 1- or Iba1-expressing macrophages, and mucosal Mcpt1$^+$ mast cells (Chapman et al., 2018) (Figure S2G–I). Of note, 22-day-old *Foxp3*^{Cre}*Pggt1b*$^{fl/fl}$ mice had pronounced inflammation in all organs examined, while *Foxp3*^{Cre}*Fntb*$^{fl/fl}$ mice showed inflammation only in the liver, lung, and skin (Figure 2D). Thus, ablation of either Fntb or Pggt1b in T_{reg} cells leads to the development of a fatal and early-onset autoimmune disease.

Analysis of immune homeostasis revealed increased percentages of effector/memory CD4$^+$ and CD8$^+$ T cells in the spleen of 3-week-old *Foxp3*^{Cre}*Fntb*$^{fl/fl}$ (Figure 2E) and *Foxp3*^{Cre}*Pggt1b*$^{fl/fl}$ mice (Figure 2F). These mutant mice also had elevated percentages of splenic CD4$^+$ T cells producing IFN-γ and IL-4, and CD8$^+$ T cells expressing IFN-γ (Figure 2G and H), while IL-17-producing CD4$^+$ T cells were significantly increased in *Foxp3*^{Cre}*Fntb*$^{fl/fl}$ mice only (Figure 2G and H). However, activation and cytokine production by T cells were not elevated in 7-day-old neonatal *Foxp3*^{Cre}*Fntb*$^{fl/fl}$ mice (Figure S2J and K), whereas *Foxp3*^{Cre}*Pggt1b*$^{fl/fl}$ mice had markedly enhanced T-cell activation (Figure S2L), IFN-γ production from CD4$^+$ and CD8$^+$ T cells (Figure S2M), and increased IL-17- and IL-4-producing CD4$^+$ T cells (Figure S2M). These differences in early immune cell activation are consistent with the more rapid lethality of *Foxp3*^{Cre}*Pggt1b*$^{fl/fl}$ compared with *Foxp3*^{Cre}*Fntb*$^{fl/fl}$ mice (Figure 2B), as well as the stronger defect in the suppressive activity of Pggt1b-deficient T_{reg} cells as compared to those lacking Fntb (Figure S2E and F). Collectively, these results show that Fntb and Pggt1b in T_{reg} cells control immune homeostasis, with a more important role of Pggt1b for establishing immune tolerance in the neonatal stage.

Fntb and Pggt1b are essential for eT_{reg}-cell accumulation

Reduced T_{reg}-cell number can provoke autoimmunity (Savage et al., 2020). Accordingly, the percentage and number of T_{reg} cells were decreased in *Foxp3*^{Cre}*Fntb*$^{fl/fl}$ (Figure S3A) and *Foxp3*^{Cre}*Pggt1b*$^{fl/fl}$ mice (Figure S3B) at 3-weeks of age. To circumvent the possible secondary effects due to the inflammatory environment, we generated mixed bone marrow chimeras (see Methods) as a cell-intrinsic system, wherein the presence of WT T_{reg} cells (CD45.1$^+$) prevents the development of inflammation (Zeng et al., 2013). The frequency and number of T_{reg} cells lacking Fntb (Figure 3A) or Pggt1b (Figure 3B) were reduced in the chimeras, indicating the cell-autonomous roles of these molecules. In contrast, Foxp3

expression on a per cell basis was not altered in Fntb- or Pggt1b-deficient T_{reg} cells from these chimeras (Figure 3C and D) or *Foxp3*^{Cre}*Fntb*$^{fl/fl}$ (Figure S3C) and *Foxp3*^{Cre}*Pggt1b*$^{fl/fl}$ mice (Figure S3D). Fntb- and Pggt1b-deficient T_{reg} cells had cell-intrinsic reduction of survival [as indicated by 7AAD or fixable live-dead viability (FVD) dye] under homeostasis (Figure S3E and F) and after activation *in vitro* (Figure S3G and H), indicating that Fntb and Pggt1b are not required for the stability of Foxp3 expression but contribute to cell survival.

To explore Fntb- or Pggt1b-dependent functional programs, we performed transcriptome analysis of CD45.2^{+} T_{reg} cells isolated from mixed bone marrow chimeras. Differential expression (DE) analysis revealed 52 upregulated and 162 downregulated genes in T_{reg} cells lacking Fntb, and 271 upregulated and 304 downregulated genes in those deficient in Pggt1b-(Figure 3E). Fold-change/fold-change (FC/FC) plot analysis showed that 51 genes were downregulated in both Fntb- and Pggt1b-deficient T_{reg} cells (Figure 3F), including 40 eT_{reg} cell-associated genes (Levine et al., 2014). In fact, out of 448 eT_{reg} signature genes (Levine et al., 2014) (see Methods), 123 and 189 were significantly downregulated in Fntb- or Pggt1b-deficient T_{reg} cells, respectively (Figure 3G), suggesting that Fntb and Pggt1b orchestrate the transcriptional program of eT_{reg} cells.

Consistent with reduced eT_{reg}-cell signatures, there were decreased frequency and number of CD44^{hi}CD62L^{lo} eT_{reg} cells in 3-week-old *Foxp3*^{Cre}*Fntb*$^{fl/fl}$ (Figure 3H) and *Foxp3*^{Cre}*Pggt1b*$^{fl/fl}$ (Figure 3I) mice, as well as reduced number, but increased frequency, of cT_{reg} cells (Figure S3I and J), associated with reduced survival of both cT_{reg} and eT_{reg} cells (Figure S3K and L). However, there was a more pronounced decrease in the number of eT_{reg} than cT_{reg} cells (Figure S3M and N). Analysis of T_{reg}-cell subsets in mixed bone marrow chimeras revealed cell-autonomous defects in eT_{reg}-cell accumulation (Figure 3J and K). We also generated *Foxp3*$^{Cre/wt}$*Fntb*$^{fl/fl}$ or *Foxp3*$^{Cre/wt}$*Pggt1b*$^{fl/fl}$ mice (called ‘mosaic’ mice), where *Foxp3*^{Cre} is expressed in 50% of T_{reg} cells due to random inactivation of the X-chromosome that bears the *Foxp3* gene; analysis of these mice also revealed a reduction of eT_{reg} cells (Figure S3O and P). Hmgcr deficiency similarly reduced eT_{reg}-cell accumulation in *Foxp3*^{Cre}*Hmgcr*$^{fl/fl}$ mice (Figure S3Q) and mixed bone marrow chimeras (Figure S3R), associated with altered immune homeostasis and fatal autoimmunity observed in *Foxp3*^{Cre}*Hmgcr*$^{fl/fl}$ mice (Lacher et al., 2017). Non-lymphoid tissues, such as the liver and lung, are enriched for eT_{reg} cells (Whibley et al., 2019), and neonatal *Foxp3*^{Cre}*Fntb*$^{fl/fl}$ and *Foxp3*^{Cre}*Pggt1b*$^{fl/fl}$ mice had reduced numbers of T_{reg} cells in these organs (Figure 3L and M). Further, Fntb- or Pggt1b-deficient cT_{reg} and eT_{reg} cells isolated from mixed bone marrow chimeras had lower expression of ICOS and CTLA4 (Figure S3S and T). In contrast, CD25 expression was increased on Fntb-deficient cT_{reg} and eT_{reg} cells (Figure S3S) and not altered on Pggt1b-deficient cT_{reg} but trending increased on Pggt1b-deficient eT_{reg} cells (Figure S3T). eT_{reg} cells are also more proliferative *in vivo* (Smigiel et al., 2014) and Fntb- and Pggt1b-deficient T_{reg} cells displayed reduced proliferation as indicated by Ki67 staining (Figure 3N and O). Thus, Fntb and Pggt1b are essential for eT_{reg} cell-accumulation *in vivo*.

Fntb and Pggt1b regulate distinct aspects of eT_{reg}-cell homeostasis

While both Fntb and Pggt1b were essential for eT_{reg}-cell accumulation, there were pronounced differences in the inflammatory status of neonatal *Foxp3*^{Cre}*Fntb*$^{fl/fl}$ and *Foxp3*^{Cre}*Pggt1b*$^{fl/fl}$ mice (Figure S2J–M). Also, *Foxp3*^{Cre}*Fntb*$^{fl/fl}$ mice had reduction of eT_{reg} cells beginning at 2 weeks, but not on day 7, after birth (Figure 4A), whereas eT_{reg}-cell accumulation in *Foxp3*^{Cre}*Pggt1b*$^{fl/fl}$ mice was impaired at all time points examined (Figure 4B). To determine if Fntb and Pggt1b differentially promote cT_{reg}-cell activation and differentiation into eT_{reg} cells, we purified CD44^{lo}CD62L^{hi} cT_{reg} cells and stimulated them with anti-CD3/28 and IL-2 to promote their activation and differentiation into CD44^{hi}CD62L^{lo} eT_{reg}-like cells (Luo et al., 2016). We found that eT_{reg}-like cell generation among CTV^{lo} cells (Figure 4C) or expression of activation or suppressive molecules (Figure S4A) was largely unaltered in the absence of Fntb. In contrast, eT_{reg}-like cell generation was reduced in Pggt1b-deficient cells (Figure 4D), associated with impaired expression of activation or suppressive molecules (Figure S4B). Similar effects were observed when cT_{reg} cells from inflammation-free ‘mosaic’ mice were used (Figure S4C and D). Simvastatin-treated cT_{reg} cells also had reduced eT_{reg}-like cell generation that was rescued by GGPP but not FPP, demonstrating an essential role for GGPP in promoting eT_{reg}-cell differentiation (Figure 4E). Thus, Fntb is dispensable for cT_{reg}-cell activation and differentiation into eT_{reg} cells but may contribute to eT_{reg}-cell maintenance, whereas Pggt1b promotes eT_{reg}-cell differentiation during cT_{reg}-cell activation.

The above FC/FC plot analysis revealed that 406 (253 upregulated and 153 downregulated) genes were altered selectively in Pggt1b-deficient T_{reg} cells as compared with Fntb-deficient T_{reg} cells (Figure S4E), suggesting possible mechanistic differences for Fntb and Pggt1b in eT_{reg}-cell accumulation. To test the contributions and mechanisms of Fntb and Pggt1b activities in eT_{reg}-cell accumulation and to circumvent the effects of steady-state eT_{reg}-cell defects in the absence of Fntb or Pggt1b, we stimulated cT_{reg} cells with anti-CD3/28 and IL-2 in the presence of vehicle, FTI or GGTI, to acutely inhibit Fntb or Pggt1b, respectively (Wang and Casey, 2016). FTI showed the expected selective inhibition of the farnesyltransferase, while GGTI selectively impaired the function of the geranylgeranyltransferase type 1 (Figure S4F). FTI and GGTI treatments also recapitulated the respective lack of and inhibitory effects on eT_{reg}-like cell generation described above for mutant cells (Figure S4G and H), validating this system.

To unbiasedly identify gene modules regulated by Fntb and Pggt1b activities, we performed transcriptome profiling of cT_{reg} cells stimulated with TCR in the presence of vehicle, FTI or GGTI, followed by weighted gene correlation network analysis (WGCNA) (Tan et al., 2017). First, we identified four clusters that were upregulated upon activation in the vehicle-treated control cells (clusters 1, 3, 7, and 8): genes in cluster 1 were induced relatively independently of farnesyltransferase and geranylgeranyltransferase type 1 activity, while those in clusters 3, 7, and 8 were not fully upregulated upon FTI treatment and were markedly downregulated in GGTI-treated cells across time (Figure 4F). Second, clusters 2 and 4 contained gene profiles that were downregulated upon activation in vehicle control cells, with inhibition of Pggt1b, and to a lesser extent, Fntb, preventing activation-induced repression of these gene signatures (Figure 4F). In fact, cluster 4 had genes that were

increased in expression at 48 h by GGTI treatment. Finally, clusters 5 and 6 were relatively unchanged across activation in vehicle controls. Treatment with FTI and GGTI increased expression of genes in cluster 5, whereas reduction of gene signatures in the presence of these inhibitors were observed in cluster 6 (Figure 4F). Thus, Fntb and Pggt1b activities regulate largely distinct transcriptional programs upon TCR stimulation, with a more pronounced effect induced by Pggt1b inhibition.

Functional enrichment analysis revealed that cluster 1, which was modestly altered by FTI or GGTI treatment, was enriched with genes in cell-cycle regulation, certain anabolic pathways and apoptosis (Figure 4F and G), and we validated that FTI and GGTI treatments reduced cell proliferation and survival during activation (Figure S4I and J). Clusters 2, 4, and 5 were upregulated upon GGTI treatment as compared with either DMSO or FTI treatment at 48 h, and were enriched for IL-2-STAT5 signaling or pathways associated with inflammation or hypoxia (Figure 4F and H). In contrast, in clusters 3, 6, and 7, where gene expression was downregulated in GGTI-treated cells, had altered pathways related to eT_{reg}-cell differentiation, including mTORC1 and NF-κB signaling (Chapman et al., 2018; Oh et al., 2017; Sun et al., 2018; Vasanthakumar et al., 2017) (Figure 4F and H). Cluster 8 represented a small subset of genes enriched in NF-κB signaling, including *Atf3* (Figure 4F and H). Thus, WGCNA and functional enrichment reveal that Fntb and Pggt1b activities mediate selective gene expression programs underlying the function and activation of T_{reg} cells.

Fntb maintains eT_{reg}-cell subsets via mTORC1 and ICOS signaling

To explore the mechanism of Fntb-dependent eT_{reg}-cell maintenance, we performed GSEA of the transcriptome of TCR-activated cT_{reg} cells treated with FTI, which showed decreased gene signatures associated with mTORC1 activation (Figure 5A). Next, we assessed the phosphorylation of two mTORC1-dependent targets, ribosomal protein S6 (p-S6) and 4EBP1 (p-4EBP1) by flow cytometry. p-S6 and p-4EBP1 levels were reduced in FTI-treated cT_{reg} cells after TCR stimulation (Figure 5B), which was further verified by immunoblot analysis of p-S6 and p-4EBP1, with a greater reduction of mTORC1 at 48 h (Figure 5C). Similar reduction of p-S6 was obtained using Fntb-deficient cT_{reg} cells isolated from 2-week-old *Foxp3*^{Cre}*Fntb*$^{fl/fl}$ mice (Figure 5D) or inflammation-free *Cd4*^{Cre}*Fntb*$^{fl/fl}$ mice (Figure 5E). In contrast, deletion of Pggt1b or its inhibition by GGTI had no effect on mTORC1 signaling under the same activation conditions (Figure S5A and B). Thus, Fntb, but not Pggt1b, is essential for mTORC1 activation and downstream metabolic events in TCR-stimulated cT_{reg} cells.

To test the contribution of reduced mTORC1 signaling to impaired Fntb-deficient eT_{reg}-cell accumulation, we bred *Cd4*^{Cre}*Fntb*$^{fl/fl}$ mice with *Tsc1*$^{fl/fl}$ mice that have hyper-activation of mTORC1 signaling (Yang et al., 2011). Co-deletion of Tsc1 largely restored the frequency of eT_{reg} cells (Figure 5F) and completely restored T_{reg}-cell proliferation *ex vivo* (Figure 5G) and *in vitro* (Figure S5C) as compared with *Cd4*^{Cre}*Fntb*$^{fl/fl}$ mice. However, co-deletion of Tsc1 did not rescue cellular survival (Figure S5D). We then considered other signaling pathways that may promote T_{reg}-cell survival *in vivo*. Fntb-deficient or FTI-treated cT_{reg} cells had impaired activation-induced ICOS expression (Figure 5H and I and Figure S5E),

and co-deletion of Tsc1 did not appreciably increase ICOS expression on these cells (Figure S5F). Among eT_{reg} cells, ICOS expression was increased on $Bcl2^{lo}$ eT_{reg} cells than $Bcl2^{hi}$ eT_{reg} cells (Figure 5J), consistent with the role of ICOS for maintaining $Bcl2^{lo}$ T_{reg} cells *in vivo* (Smigiel et al., 2014). Accordingly, there was a reduction of the percentage and number of $Bcl2^{lo}$ eT_{reg} cells in *Foxp3*^{Cre}*Fntb*$^{fl/fl}$ mice (Figure 5K). In the $Bcl2^{lo}$ eT_{reg}-cell subset, Mcl1 expression was reduced and Bim expression was largely unchanged on a per cell basis (Figure 5L). Thus, Fntb regulates the expression of Mcl1 in the $Bcl2^{lo}$ eT_{reg}-cell subset, which likely contributes to their maintenance. To explore the mechanisms by which ICOS expression is regulated, we analyzed *Icos* expression, which was reduced in Fntb-deficient cT_{reg} cells after TCR stimulation (Figure 5M). *Icos* is a target of IRF4 (Cretney et al., 2011; Zheng et al., 2009), but IRF4 expression was not reduced in Fntb-deficient cT_{reg} cells after TCR stimulation (Figure S5G). Therefore, we performed transposase-accessible chromatin using sequencing (ATAC-Seq) assay (Buenrostro et al., 2013) with cT_{reg} or eT_{reg} cells isolated from WT or *Foxp3*^{Cre}*Fntb*$^{fl/fl}$ mixed bone marrow chimeras to identify mechanisms of *Icos* regulation. Unsupervised clustering using principal component analysis (PCA) or sample distance plot analysis showed that WT cT_{reg} and eT_{reg} cells showed distinct chromatin accessibility profiles (Figure 5N and Figure S5H), indicative of extensive remodeling of the chromatin state between these T_{reg}-cell subsets. Further, Fntb-deficient eT_{reg} cells had considerably altered chromatin profiles as compared to WT eT_{reg} cells, whereas WT and Fntb-deficient cT_{reg} cells had more modest differences (Figure 5N and Figure S5H). Transcription factor motif searches in differentially accessible regions of ATAC-Seq (Karmaus et al., 2019; Wei et al., 2019) showed that Fntb-deficient cT_{reg} and eT_{reg} cells had markedly reduced accessibility in regions corresponding to SP family members (SP1–SP4), as well as selective AP-1 family members, including Batf and Jun (Figure 5O and Figure S5I). These results reveal the importance of Fntb in mediating the chromatin state of eT_{reg} cells, including a role in regulating Jun activity that likely contributes to ICOS expression (Koizumi et al., 2018).

To establish the functional relevance of ICOS, we generated retrogenic mice using bone marrow cells from WT or *Cd4*^{Cre}*Fntb*$^{fl/fl}$ mice transduced with empty control (pMIG) or ICOS-expressing vector. ICOS overexpression restored ICOS expression on Fntb-deficient T_{reg} cells (Figure S5J) and partially rescued eT_{reg}-cell frequency and number (Figure 5P). Collectively, these data suggest that mTORC1 and ICOS act as two largely separate pathways to mediate Fntb-dependent eT_{reg}-cell maintenance, where mTORC1 signaling sustains cellular proliferation and ICOS promotes survival of $Bcl2^{lo}$ eT_{reg} cells.

Pggt1b acts as a rheostat for TCR signaling

We performed ATAC-Seq analysis (Buenrostro et al., 2013) of cT_{reg} or eT_{reg} cells from WT or *Foxp3*^{Cre}*Pggt1b*$^{fl/fl}$ mixed bone marrow chimeras for mechanistic insights. Unbiased clustering analyses showed that the chromatin accessibility profiles of Pggt1b-deficient cT_{reg} cells were only modestly different as compared to WT cT_{reg} cells, whereas Pggt1b-deficient eT_{reg} cells were distinct and did not resemble either WT cT_{reg} or eT_{reg} cells (Figure 6A and B). Thus, Pggt1b is important for chromatin remodeling in eT_{reg} cells and, to a lesser extent, cT_{reg} cells. Transcription factor motif searches showed that Pggt1b-deficient eT_{reg} cells had markedly reduced accessibility in regions corresponding to Jun and Fos (AP-1 family)

binding sites (Figure 6C and D and Figure S6A), which were enriched in WT eT_{reg} cells than cT_{reg} cells (Figure S6B). NFAT and NF-κB binding sites were also downregulated, albeit to a lesser extent than AP-1 factors (Figure S6A), raising the possibility of reduced TCR signaling in these cells. Odds ratio/odds ratio plot analysis of transcription factor binding motifs of Fntb- and Pggt1b-deficient cT_{reg} or eT_{reg} cells showed that the predicted transcriptional regulators were largely discrete between them, with the exception of Batf or Jun family members that are important eT_{reg}-cell regulators (Figure S6C) (Koizumi et al., 2018; Vasanthakumar et al., 2015). As AP-1 activity is associated with TCR signal strength (Koizumi et al., 2018), we examined TCR signal strength using the surrogates CD5 and Nur77-GFP. GGTI treatment suppressed the upregulation of CD5 and Nur77-GFP upon TCR activation of cT_{reg} cells (Figure 6E), suggesting that Pggt1b tunes TCR signals.

To receive TCR signals *in vivo,* T_{reg} cells interact with antigen-presenting dendritic cells (DCs) in the T-cell zone (Li and Rudensky, 2016). Accordingly, Pggt1b-deficient T_{reg} cells had reduced adhesion to DCs, with a more pronounced defect observed in eT_{reg} cells (Figure 6F). To examine if Pggt1b promotes T_{reg}-cell localization to the T-cell zone, injected WT or *Foxp3*$^{Cre/wt}$*Pggt1b*$^{fl/fl}$ 'mosaic' mice with anti-CD4-PE (Shi et al., 2018;Smigiel et al., 2014). Pggt1b-deficient Foxp3^{+}YFP^{+} T_{reg} cells were preferentially accumulated in the splenic red pulp/marginal zone (RP/MZ) and reduced in the white pulp (WP; corresponding to the T-cell zone) compared to WT Foxp3^{+}YFP^{+} cells (Figure 6G). Thus, Pggt1b is critical for promoting T_{reg}-cell adhesion to DCs that is permissive for TCR signals and for driving their accumulation in the T-cell zone.

Rac signaling is essential for eT_{reg}-cell accumulation and immune tolerance

To identify possible molecular targets of Pggt1b, we used ingenuity pathway analysis, which predicted that several canonical pathways were downregulated in Pggt1b-deficient T_{reg} cells including Rac signaling (Figure S7A). To establish the physiological function of Rac signaling in T_{reg} cells, we generated *Foxp3*^{Cre}*Rac1*$^{fl/fl}$*Rac2*$^{-/-}$ mice, which developed enlarged secondary lymphoid tissues by day 14 after birth (Figure 7A), associated with an increase of effector/memory CD4^{+} and CD8^{+} T cells in the spleen and pLN (Figure 7B). eT_{reg} cells were reduced in the absence of Rac1/2 (Figure 7C), which was verified to be cell-intrinsic using *Foxp3*$^{Cre/wt}$*Rac1*$^{fl/fl}$*Rac2*$^{-/-}$ 'mosaic' mice (Figure 7D). Also, Rac1/2-deficientc T_{reg} cells had reduced capacity to differentiate into eT_{reg}-like cells after *in vitro* TCR stimulation (Figure S7B), associated with lower CD44 but higher CD62L expression (Figure S7C). Rac1/2-deficient cT_{reg} and eT_{reg} cells also had reduced adhesion to DCs (Figure 7E). To establish a direct link between Pggt1b and dysfunctional Rac signaling, we expressed a constitutively active form of Rac1 (Rac1 G12V) in WT cT_{reg}, followed by TCR stimulation in the presence of different doses of GGTI and analysis of eT_{reg}-like cell differentiation. Expression of Rac1 G12V partially restored the frequency of eT_{reg}-like cells at different doses of GGTI treatment (Figure 7F). These results indicate that Rac signaling contributes to TCR-dependent activation and eT_{reg}-cell differentiation downstream of Pggt1b.

Discussion

eT_{reg}-cell programming enforces immune tolerance under steady state and in pathological conditions. Emerging studies highlight metabolic programs in T_{reg}-cell function (Galgani et al., 2016; Newton et al., 2016), but how metabolic pathways regulate their differentiation and persistence, especially at the level of intracellular signaling, is underexplored. Here we established bidirectional metabolic signaling between immunoreceptor signaling and metabolism-dependent posttranslational lipid modifications in eT_{reg}-cell differentiation and maintenance. Specifically, isoprenoids derived from the mevalonate metabolic pathway establish activated T_{reg}-cell suppressive activity, and isoprenoid-dependent protein farnesylation and geranylgeranylation in T_{reg} cells are required for immune tolerance. Further, we identified specific promoting effects of Fntb on mTORC1 activity and ICOS expression for eT_{reg}-cell maintenance, and Pggt1b for mediating TCR activation and Rac signaling for eT_{reg}-cell differentiation. Thus, our studies identify a critical link between cellular metabolism and protein posttranslational lipid modifications necessary for the differentiation and maintenance of eT_{reg} cells.

T_{reg} cells acquire different metabolic programs associated with their activation states (Chapman et al., 2018; Sun et al., 2018; Wei et al., 2016), but how these programs regulate T_{reg}-cell subset differentiation and function is poorly understood. We found that T_{reg} cells undergoing TCR activation upregulate several genes in the mevalonate pathway to generate FPP and GGPP and promote activated T_{reg}-cell suppressive activity. Downstream of the mevalonate–isoprenoid pathway, Fntb and Pggt1b orchestrate eT_{reg}-cell accumulation and absence of Fntb or Pggt1b in T_{reg} cells leads to the development of fatal autoimmunity, consistent with the notion that Hmcgr deficiency also reduces eT_{reg}-cell accumulation *in vivo* and suppressive function associated with development of autoimmunity (Lacher et al., 2017; Zeng et al., 2013). Notably, mevalonate metabolism may also influence eT_{reg}-cell accumulation via cholesterol biosynthesis essential for T-cell proliferation (Kidani et al., 2013) or by mitochondrial ubiquinone synthesis (Mullen et al., 2016). While isoprenoids are biochemically similar lipid molecules (Berndt et al., 2011), we found that Fntb and Pggt1b serve discrete cellular functions, with Fntb maintaining the eT_{reg}-cell homeostasis by sustaining mTORC1-dependent proliferation as well as expression of ICOS, whose signaling regulates the survival of ICOS-expressing $Bcl2^{lo}$ eT_{reg} cells (Smigiel et al., 2014). In contrast, ablation of Pggt1b selectively abolishes eT_{reg}-cell induction (Smigiel et al., 2014). These findings are consistent with our observations that expression of *Pggt1b*, but not *Fntb*, is upregulated during initial T_{reg}-cell activation. Thus, we have uncovered discrete roles for Fntb and Pggt1b in eT_{reg}-cell maintenance and differentiation, highlighting posttranslational lipid modifications as crucial, temporal regulators for eT_{reg}-cell accumulation and function.

Upon TCR stimulation, mTORC1 promotes anabolic metabolism to allow for quiescence exit and programming of effector-like T-cell subsets (Tan et al., 2017; Yang et al., 2013), including eT_{reg} cells (Chapman et al., 2018; Sun et al., 2018). More recently, studies indicated that metabolic pathways regulate mTORC1 signaling. For instance, autophagy is selectively active in eT_{reg} cells and restrains mTORC1 activity to enforce their lineage stability and survival (Wei et al., 2016). These results suggest that eT_{reg}-cell fitness is mediated by the interplay between mTORC1 and anabolic metabolism. We identified Fntb,

but not Pggt1b, as an upstream regulator of mTORC1 activity in T_{reg} cells. Of note, Fntb deficiency partially reduces mTORC1 activity at later time points but is insufficient to block eT_{reg}-cell differentiation, unlike ablation of mTOR activity (Chapman et al., 2018). Thus, our data suggest that Fntb may be more important for sustaining mTORC1 activation. In this regard, mTORC1 activity induces expression of mevalonate-pathway enzymes (Zeng et al., 2013), suggesting a bidirectional signaling network, whereby mTORC1 induces FPP generation to mediate protein farnesylation, which in turn sustains mTORC1 activity in eT_{reg} cells.

Several transcription factors have been shown to promote eT_{reg}-cell programming (Cretney et al., 2011; Oh et al., 2017; Vasanthakumar et al., 2017; Vasanthakumar et al., 2015). Also, mitochondrial metabolism regulates transcription via epigenetic pathways (Weinberg et al., 2019), but additional mechanisms by which metabolism influences signaling or transcriptional activity, especially for eT_{reg}-cell commitment, are underexplored. We found that Pggt1b is essential for regulating TCR signal strength and AP-1 activity, which drives eT_{reg}-cell accumulation (Koizumi et al., 2018). Also, Rac signaling is crucial for TCR-dependent eT_{reg}-cell differentiation and immune tolerance *in vivo*. The mechanism by which Pggt1b affects Rac function remains unclear, but may involve regulation of its expression (Akula et al., 2019). Also, other protein geranylgeranylation targets, such as Cdc42 (Du et al., 2020), may contribute to T_{reg}-cell programming. Together, our observations indicate that metabolism-related posttranslational modifications are rheostats for the maintenance and differentiation of eT_{reg} cells.

In summary, we identified a role for metabolism-driven posttranscriptional lipid modifications in selectively shaping downstream pathways to balance key immunological signaling networks for eT_{reg}-cell maintenance and differentiation. The identification of discrete posttranslational modifications as critical and distinct regulators of T_{reg}-cell function highlights therapeutic possibilities for targeting these pathways in diseases. We also provide mechanisms for the temporal regulation of TCR signaling and mTORC1 and Rac activities that dictate eT_{reg}-cell accumulation. From this prospective, the observations that Fntb and Pggt1b regulate distinct signaling pathways and cellular functions may provide opportunities to selectively modulate T_{reg}-cell activity in autoimmune, cancer, and infectious diseases.

Limitations of study

While our study provides strong evidence for Pggt1b and Fntb as temporal regulators of eT_{reg}-cell homeostasis, T_{reg}-cell survival is defective in the absence of these molecules, the mechanistic basis of which remains unknown. We have established that Pggt1b and Fntb mediate murine T_{reg}-cell suppressive function and immune tolerance *in vivo*. However, whether these effects extend to human T_{reg} cells remains to be explored. Further, our data reveal the inhibitory effects of simvastatin or Hmgcr deletion on T_{reg}-cell activation and suppressive activity. While cholesterol appears to be dispensable for these processes, whether other mevalonate-derived metabolites contribute to T_{reg}-cell regulation is unknown.

STAR*METHODS

RESOURCE AVAILABILITY

Lead contact—Further information and requests for resources and reagents should be directed to and will be fulfilled by the Lead Contact, Hongbo Chi (hongbo.chi@stjude.org).

Materials availability—Plasmids and mouse lines generated in this study are available on request from the Lead Contact, Hongbo Chi (hongbo.chi@stjude.org) and submission of appropriate Materials Transfer Agreements.

Data and code availability—The accession number for the microarray data of $CD4^+YFP^+$ WT and Fntb- or Pggt1b-deficient T_{reg} cells from mixed bone marrow chimeras reported in this paper is GSE158863. The accession number for the microarray data of $CD4^+YFP^+$ cT_{reg} cells treated with FTI or GGTI and stimulated with anti-CD3/28 plus IL-2 for different times in this paper is GSE158863. The accession number for the ATAC-Seq data of $CD4^+YFP^+$ WT and Fntb- or Pggt1b-deficient cT_{reg} and eT_{reg} cells from mixed bone marrow chimeras reported in this paper is GSE158863.

EXPERIMENTAL MODEL AND SUBJECT DETAILS

Mice—*Rag1*$^{-/-}$, CD45.1$^+$, *Cd4*^{Cre}, *Tsc1*$^{fl/fl}$, *Rac1*$^{fl/fl}$, *Rac2*$^{-/-}$, Foxp3-RFP, Nur77-GFP and C57BL/6 mice were purchased from the Jackson Laboratory. *Fntb*$^{fl/fl}$ and *Pggt1b*$^{fl/fl}$ mice were kind gifts from M. Bergo (Khan et al., 2011; Liu et al., 2010). *Foxp3*^{Cre} mice were from A. Rudensky (Rubtsov et al., 2008). All genetic models were on the C57BL/6 background. Both male and female mice were used for analysis and quantification. *Foxp3*^{Cre}*Fntb*$^{fl/fl}$ and *Foxp3*^{Cre}*Pggt1b*$^{fl/fl}$ mice were used at various ages as indicated in figure legends, with age- and gender-matched *Foxp3*^{Cre}*Fntb*^{wt} or *Foxp3*^{Cre}*Fntb*$^{fl/wt}$ and *Foxp3*^{Cre}*Pggt1b*^{wt} or *Foxp3*^{Cre}*Pggt1b*$^{fl/wt}$ mice as controls (indicated as WT in figure legends). All mice were kept in a specific pathogen-free facility in the Animal Resource Center at St. Jude Children's Research Hospital. Mice were housed up to 5 mice per cage in a temperature- (25–25 °C) and humidity-controlled colony room maintained on a 12 h light/dark cycle (06:00–18:00 light on). Standard chow (Purina LabDiet® Autoclavable Rodent Breeder Diet #5013) and water were provided *ad libitum*. The health status of mice was monitored by trained husbandry staff or researchers at least once daily. Animal protocols were approved by the Institutional Animal Care and Use Committee of St. Jude Children's Research Hospital.

METHOD DETAILS

Mixed bone marrow chimera generation—Bone marrow cells isolated from tibia and femur were used to generate mixed bone marrow chimeras, by transferring 2×10^6 T cell-depleted $CD45.2^+$ bone marrow cells from *Foxp3*^{Cre}*Fntb*$^{fl/fl}$ or *Foxp3*^{Cre}*Pggt1b*$^{fl/fl}$ mice (or their sex-matched littermate controls) and $CD45.1^+$ WT bone marrow cells at ratio of 1:1 into sub-lethally irradiated (5 Gy) *Rag1*$^{-/-}$ mice. Mice were analyzed at 7–8 weeks after reconstitution.

Retrogenic mouse generation—To generate retrogenic mice, bone marrow cells from the femur and tibia of WT or inflammation-free *Cd4*^{Cre}*Fntb*$^{fl/fl}$ mice were enriched for lineage-negative (Lin^{-}) cells using the Lineage Cell Depletion kit (Miltenyi Biotec). The cells were cultured in Dulbecco's modified essential medium (DMEM) supplemented with 20% fetal bovine serum (FBS), recombinant human IL-6 (50 ng/ml), murine IL-2 (20 ng/ml), and murine stem cell factor (SCF, 50 ng/ml) for 2 days. Retroviruses were produced by transfecting Plat-E cells with the pMIG or pMIG-ICOS-OE (Sino Biological) retroviral vectors. Retrovirus (MOI: 10–20) was preloaded onto retronectin-coated plate by centrifugation at 1,000× *g* for 2 h at 4 °C. Bone marrow cells pre-activated with IL-3, IL-6 and SCF for 48 h were centrifuged onto the plates preloaded with retrovirus at 2,500 rpm for 2 h at room temperature and incubated for another 24 h at 37 °C. Transduced bone marrow cells were harvested and injected into sub-lethally irradiated (5 Gy) *Rag1*$^{-/-}$ mice for reconstitution. Bleeding and analysis were performed at 8 weeks after reconstitution.

Flow cytometry—For analysis of surface markers, cells were stained in PBS containing 2% (wt/vol) bovine serum albumin (BSA), with anti-CD4 (RM4–5), anti-CD4 (RM4–4), anti-CD5 (53–7.3), anti-CD8α (53–6.7), anti-TCRβ (H57–597), anti-CD44 (1M7), anti-CD62L (MEL-14), anti-CD69 (H1.22F3), anti-CD45.1 (A20), anti-CD45.2 (104), anti-CD25 (PC61.5), anti-ICOS (7E.17G9), anti-CTLA4 (UC10–4F10–11), anti-CD73 (TY/11.8), anti-CXCR3 (CXCR3–173), and anti-KLRG1 (2F1/KLRG1) (Tonbo Biosciences or eBioscience). Intracellular Foxp3 (FJK-16s), Ki67 (SolA15), IFN-γ (XMG1.2), IL-4 (11B11), IL-17 (17B7), Mcl1 (LVUBKM; all from eBioscience), Bcl2 (BCL/10C4, Biolegend), Bim (C34C5), p-S6 (D57.2.2E), and p-4EBP1 (236B4; all from Cell Signaling Technology) were analyzed by flow cytometry according to the manufacturer's instructions. For intracellular cytokine staining, splenocytes containing T cells were stimulated for 4 h with PMA and ionomycin in the presence of monensin before intracellular staining according to the manufacturer's instructions (eBioscience). For phospho-flow staining, the cells were stained with FVD and fixed by phospho-flow buffers (BD Biosciences) before performing intracellular staining. To monitor cell division and cell death, lymphocytes were labeled with CTV (2.5 μM; Life Technologies) and FVD per the manufacturer's instructions. Flow cytometry data were acquired on LSR Fortessa or LSRII (BD Biosciences) and analyzed using FlowJo software (Tree Star).

Pathology and immunohistochemistry—All tissues were fixed in formalin, embedded in paraffin, sectioned at 4 μm, mounted on positively charged glass slides (Superfrost Plus; Thermo Fisher Scientific), and dried at 60 °C for 20 min before dewaxing and staining with hematoxylin and eosin (H&E) using standard methods. For immunohistochemical staining, the primary antibodies included the following: for T cells, anti-CD4 (1:40 dilution, Cat # 14–9766; Thermo Fisher) and anti-CD8 (1:40 dilution, Cat # 14–0808-82; Thermo Fisher); for macrophages, anti-Iba1 (1:300 dilution, Cat # CP290A; Biocare Medical) and anti-arginase 1 (1:40 dilution, Cat # sc-20150; Biocare Medical); and anti-Mcpt1 monoclonal antibody for interepithelial mucosal mast cells (1:30 dilution, Cat # 14–55303-82, eBioscience). For detection of CD4 and Mcpt1, sections underwent antigen retrieval at 100 °C for 20 min in Epitope Retrieval solution 2 (ER2) on a Bond Max immunostainer (Leica Biosystems). Then biotinylated secondary rabbit anti-rat antibody diluted 1:400 (BA-4001;

Vector Laboratories) was applied for 10 min, followed by Bond polymer refine detection kit with 3,3'-diaminobenzidine (DAB) as chromogenic substrate and a hematoxylin counterstain (DS9800; Leica Biosystems). For detection of CD8, Iba1 and arginase 1, tissue sections underwent antigen retrieval in a prediluted Cell Conditioning Solution (*CC1*) (Ventana Medical Systems) for 32 min. For anti-CD8, a biotinylated secondary rabbit anti-goat antibody (1:400 dilution; BA-5000; Vector Laboratories) was applied for 10 min, while for anti-Iba1 and anti-arginase 1, the OmniMap anti-rabbit HRP kit (Ventana Medical Systems) was used for detection. ChromoMap DAB was the chromogen for CD8, CD4, Iba1, and Mcpt1, whereas the Discovery Purple chromogen was used for arginase 1 (both from Ventana Medical Systems). All sections were examined by a pathologist blinded to the experimental group assignments (author P.V.).

Cell purification and culture—For isolation of DCs, spleens were digested with collagenase D (Worthington), followed by enrichment with CD11c microbeads (Miltenyi Biotec) and sorting for TCRβ$^-$B220$^-$CD49b$^-$ CD11c$^+$ DCs. Unless otherwise noted, lymphocytes were isolated from spleen and pLN (including inguinal, auxiliary and cervical lymph nodes), and naïve CD4$^+$ T cells (CD4$^+$ Foxp3-YFP$^-$ CD44^{lo}CD62L^{hi}), T_{reg} cells (CD4$^+$Foxp3-YFP$^+$ or CD4$^+$CD25$^+$) or cT_{reg} cells (CD4$^+$Foxp3-YFP$^+$CD44^{lo}CD62L^{hi} or CD4$^+$CD25$^+$CD44^{lo}CD62L^{hi}) from *Foxp3*^{Cre} or C57BL/6 mice were sorted on a MoFlow (Beckman-Coulter) or Reflection (i-Cyt). Sorted T_{reg} cells were cultured in plates coated with anti-CD3 (145–2C11, 10 μg/ml) and anti-CD28 (37.51; 10 μg/ml; both from Bio X Cell) antibodies for indicated times in complete Click's medium [Click's medium supplemented with β-mercaptoethanol, 10% (vol/vol) FBS, 1% (vol/vol) penicillin-streptomycin] and IL-2 (200 U/ml). All cell culture experiments were performed at 37 °C with 5% CO_2. In some experiments, GGTI-2147 (5 μM) (345885, Calbiochem), FTI-277 (10 μM) (2407, Tocris), DGBP (25 μM). cT_{reg} cells were pretreated with inhibitors for 1 h and then stimulated with 10 μg/ml anti-CD3/28 antibodies plus 200 U/ml IL-2 in the presence of inhibitors. Retrovirus containing GFP control or GFP-Rac1 G12V vector was produced in Plat-E cells as described above. For Rac1 G12V overexpression, cT_{reg} cells isolated from C57BL/6 mice were activated with 10 μg/ml anti-CD3/28 antibodies plus 200 U/ml IL-2 for 18 h, followed by spin-transduction (MOI: 10–20) at 900× *g* for 3 h at 25 °C in the presence of 10 μg/ml polybrene (Shi et al., 2018). The cells were cultured in complete Click's medium with 200 U/ml IL-2 for overnight at 37 °C. The cells were labeled with 2.5 μM CTV for 15 min, pretreated with GGTI for 1 h, and stimulated with 10 μg/ml anti-CD3/28 antibodies plus 200 U/ml IL-2 in the presence of GGTI for 3 days. Cells were harvested for flow cytometry analysis at different time points as indicated in figure legends. T_{reg}-cell suppressive assays were performed by co-culture of WT T_{reg} cells activated for 3 days with anti-CD3/28 antibodies plus IL-2 in the presence of simvastatin (2 μM) (567021, EMD Millipore) without or with mevalonate (500 μM; M4667, Sigma), FPP (20 μM; F6892, Sigma) or GGPP (5 μM; G6025, Sigma), or using purified T_{reg} cells from WT and *Foxp3*^{Cre}*Fntb*$^{fl/fl}$ or *Foxp3*^{Cre}*Pggt1b*$^{fl/fl}$ mice and naïve CD4$^+$ T cells from WT mice as previously described (Zeng et al., 2013).

***In vitro* conjugation assay—**Lymphocytes isolated from the spleen and pLN (including inguinal, auxiliary and cervical lymph nodes) and CD11c$^+$ DCs from the spleen of C57BL/6

mice were sorted as mentioned above. DCs were labeled with CTV. cT_{reg} cells ($CD4^+$Foxp3-$YFP^+CD44^{lo}CD62L^{hi}$) or eT_{reg} cells ($CD4^+$Foxp3-$YFP^+CD44^{hi}CD62L^{lo}$) (1×10^4) from *Foxp3*^{Cre} mice were cultured together with 6×10^4 DCs in a 96-well round-bottomed plate in complete Click's medium in the presence of 500 U/ml IL-2 as described previously (Levine et al., 2014). Following 10 h of co-culture at 37 °C, cell conjugates (CTV^+YFP^+) were resuspended and analyzed by flow cytometry.

***In vivo* T-cell labeling—**Anti-CD4-PE (clone RM4–4; 2 μg) was administrated to mice by *i.v.* injection, and then mice were sacrificed after 5 min of labeling (Luo et al., 2016; Shi et al., 2018). Splenocytes were analyzed by flow cytometry after surface staining with anti-CD4 (clone RM4–5) antibody. Cells restricted to the RP/MZ were identified based on co-labeling of anti-CD4-RM4–4-PE (PE^+) and anti-CD4-RM4–5, while cells in the WP were identified by single labeling with anti-CD4-RM4–5 (PE^-) by flow cytometry.

ATAC-Seq library preparation—$CD45.2^+$ cT_{reg} cells and $CD45.2^+CD4^+YFP^+CD62L^{lo}CD44^{hi}$ eT_{reg} cells were sorted from mixed bone marrow chimeras (described above). ATAC-Seq samples were prepared as previously described (Karmaus et al., 2019; Wei et al., 2019). Briefly, cells were lysed in 50 μl lysis buffer (10 mM Tris-HCl, pH 7.4, 10 mM NaCl, 3 mM $MgCl_2$, 0.1% IGEPAL CA-630) on ice for 10 min followed by centrifugation (500× *g*, 10 min, 4 °C). The supernatant was carefully discarded by pipette and the pelleted nuclei were resuspended in 50 μl transposase reaction mix (25 μl 2× TD buffer, 22.5 μl nuclease-free water, and 2.5 μl Transposase enzyme) and then incubated for 30 min at 37 °C. DNA from the Transposase reaction was cleaned up using the Qiagen MinElute kit. The barcoding reaction was amplified for 5 cycles according to manufacturer's instructions (Illumina) using the NEBNext HiFi kit and verified barcoding primers. Five μl of the barcoding reaction was used to determine the ideal remaining cycle number using KAPA SYBRFast (Kapa Biosystems) reagents and real-time PCR (Applied Biosystems 7900HT). The remaining 45 μl of sample was amplified in the same reaction mix using the optimal cycle number.

ATAC-Seq analysis—ATAC-Seq data were analyzed as described (Karmaus et al., 2019; Wei et al., 2019). In brief, 2×100-bp paired-end reads from samples were trimmed for Nextera adaptor by trimmomatic version 0.36 (parameters ILLUMINACLIP:adaptor.fa:2:30:10 LEADING:10 TRAILING:10 SLIDINGWINDOW:4:18 MINLEN:25) and then aligned to the mouse genome mm9 (downloaded from gencode release M1 (https://www.gencodegenes.org/mouse/releases.html)) by BWA (version 0.7.16a, default parameters) (Li and Durbin, 2009). Duplicated reads were labeled with Picard (version 2.9.4), and only non-duplicated paired reads were analyzed further as determined by samtools (parameter '-q 1 -F 1804' version 1.9) (Li et al., 2009). With the adjustment of Tn5 shift (reads were offset were offset by +4 bp for the sense strand and −5 bp for the antisense strand), the reads were separated into nucleosome-free, mono-, di- and trinucleosomes by fragment size. A file of bigwig was generated by using the central fragment of 80-bp and then scaled to 30×10^6 nucleosome-free reads. Several peaks, including nucleosome-free, mono-, di- and tri-nucleosomes, were observed on IGV (version 2.4.13) (Robinson et al., 2011). Samples from each group had

about 20×10^6 nucleosome-free reads on average. MACS2 was used for peak calling on each sample (with default parameters and with '–extsize 200– nomodel') (Zhang et al., 2008). To ensure reproducibility, nucleosome-free regions of each genotype were re-finalized. Peaks from each replicate were kept if they were present in at least 50% of the replicates, followed by merging of all the peaks if they overlapped by 100-bp. Nucleosome-free reads from each of samples were calculated by the bedtools (version 2.25.0) (Quinlan and Hall, 2010). To find the differentially accessible regions, raw nucleosome-free reads counts were normalized by counts per million (CPM) method implemented in DEseq2 (version 1.24.0). FDR-corrected p-value < 0.05 and fold change ($\log_2$ ratio) > 0.5 were used as cutoffs for more-accessible or less-accessible regions in *Foxp3*^{Cre}*Pggt1b*$^{fl/fl}$ samples. The differentially accessible regions in ATAC-Seq data were annotated as the nearest genes using Homer annoatePeaks.pl (version 4.9.1). For motif analysis, the regions with CPM greater than first quartile of all CPM and least variable according to their median absolute deviation (MAD) score and FDR p-value > 0.5 were used as control regions. FIMO from MEME suite (version 4.11.3, '–thresh 1e-4–motif-pseudo 0.0001') was selected for scanning motif (TRANSFAC database, only included vertebrata and not 3D structure-based) matched to the nucleosome-free regions (Bailey et al., 2009). The significantly enriched motifs were determined by comparing differentially accessible regions to the control regions using two tailed Fisher's exact test. Footprinting of transcription-factor binding sites was performed using methods and regulatory genome tools box (RGT) as described (Gusmao et al., 2016; Karmaus et al., 2019; Li et al., 2019; Wei et al., 2019).

RNA and immunoblot analysis—Real-time PCR analysis was performed with primers and probe sets from Applied Biosystems or using Power SYBR Green master mix from Life Technologies as described (Zeng et al., 2013). The ABI probes were *Pggt1b* (Mm01266356_m1), *Icos* (Mm00497600_m1) and *Actb* (Mm00607939_s1). The primers for SYBR Green real-time PCR master mix were *Fntb* (forward: 5'-AACCGCTGTATAGTCTGAGACC-3', reverse: 5'-TCTCCCTCTGCAAAATGAGCC-3'), *Hmgcr* (forward: 5'-AGCTTGCCCGAATTGTATGTG-3', reverse: 5'-TCTGTTGTGAACCATGTGACTTC-3'), *Hmgcs1* (forward: 5'-AACTGGTGCAGAAATCTCTAGC-3', reverse: 5'-GGTTGAATAGCTCAGAACTAGCC-3'), *Fnta* (forward: 5'-CCCTATGGACGACGGGTTTC-3', reverse: 5'-TGATCTGGACCACTGGGTTAG-3') and *Actb* (forward: 5'-GACAGGATGCAGAAGGAGATTACTG-3', reverse: 5'-GCTGATCCACATCTGCTGGAA-3'). Immunoblots were performed as described (Yang et al., 2011) using the following antibodies: p-S6 (2F9), p-4EBP1 (236B4; both from Cell Signaling Technology), Rap1A (C-17; Santa Cruz Biotechnology), HDJ2 (KA2A5.6; Neomarkers), β-actin (AC-15; Sigma), and β-tubulin (Cell Signaling Technology).

Gene-expression profiling and bioinformatic analysis—RNA samples purified from CD45.2$^+$ T_{reg} cells from *Foxp3*^{Cre}*Fntb*$^{fl/wt}$ (n = 4) or *Foxp3*^{Cre}*Fntb*$^{fl/fl}$ (n = 4) mixed bone marrow chimeras were analyzed with the GeneChip Mouse Gene 2.0 ST array. RNA samples purified from CD45.2$^+$ T_{reg} cells from *Foxp3*^{Cre}*Pggt1b*$^{fl/wt}$ (n = 5) or *Foxp3*^{Cre}*Pggt1b*$^{fl/fl}$ (n = 4) mixed bone marrow chimeras were analyzed with Clariom S mouse array. For other experiments, cT_{reg} cells were activated with anti-CD3/28 antibodies

(10 μg/ml) + IL-2 (200 U/ml) for 18 or 48 h in the presence of DMSO control, GGTI-2147 (5 μM) or FTI-277 (10 μM). RNA samples from these cells were analyzed with Clariom S mouse array. Differentially expressed transcripts [$|\log_2 (FC)| > 0.5$ and FDR < 0.05] were identified using linear model implemented in R package limma v.3.34.9, and the Benjamini-Hochberg method was used to estimate the FDR as described (Zeng et al., 2013). For analysis of cT_{reg} cells activated in the presence of FTI or GGTI, WGCNA (Zhang and Horvath, 2005) was performed using WGCNA R package v. 1.66. We defined co-expression clusters using differentially expressed genes [$\log_2 (FC) > 0.5$ and FDR < 0.05 in at one of the conditions]. Pearson correlation matrix was calculated using the 12 samples treated with DMSO, FTI or GGTI at 0 h or 48 h, followed by an adjacency matrix calculation, with correlation matrix raised to a power of 9 using scale-free topology criterion (Zhang and Horvath, 2005). Co-expression clusters were defined by hybrid, dynamic tree-cutting method, with minimum height for merging module set at 0.2. A consensus trend for each co-expression cluster was defined based on the first principal component (eigengene) and cluster membership was defined as Pearson correlation between individual genes and the consensus trend of the co-expression cluster. Genes were assigned to most correlated co-expression cluster with cutoff of $r > 0.7$. Each co-expression cluster was annotated using either hallmark pathways downloaded from MsigDB by right-tailed Fisher's exact test. Functional enrichment analysis was performed using right-tailed Fisher's exact test, using differentially expressed genes at the $\log_2 (FC) > 0.5$ and FDR < 0.05 cut-offs. Microarray data have been deposited into the GEO database and accession code is available upon request.

For the above transcriptome analysis or for public datasets (Arvey et al., 2014; Wakamatsu et al., 2013), gene set enrichment analysis of hallmark pathways or public datasets or literature curated pathways [TCR and eT_{reg} (Levine et al., 2014)] was performed as described (Zeng et al., 2013). The manual curation of mevalonate and cholesterol pathway genes was based on the literature (Berndt et al., 2011; Mullen et al., 2016; Wang and Casey, 2016) and included the following genes: *Acat1*, *Fnta*, *Fntb*, *Fdft1*, *Fdps*, *Ggps1*, *Hmgcr*, *Hmgcs1*, *Idi1*, *Idi2*, *Mvd*, *Mvk*, *Pmvk*, and *Pggt1b*.

QUANTIFICATION AND STATISTICAL ANALYSIS

Prism 6 software (GraphPad) was used to analyze data by two-tailed unpaired Student's *t*-test as indicated in figure legends. When multiple groups were compared, one-way ANOVA with the Tukey's test was performed as indicated in figure legends. $p < 0.05$ was considered significant, with specific p-values indicated in figures and figure legends. No method was used to test for normal distribution of data. Data are presented as mean ± s.e.m.

Supplementary Material

Refer to Web version on PubMed Central for supplementary material.

Acknowledgements

The authors acknowledge M. Bergo for *Fntb*$^{fl/fl}$ and *Pggt1b*$^{fl/fl}$ mice (Khan et al., 2011; Liu et al., 2010), A. Rudensky for *Foxp3*^{Cre} mice (Rubtsov et al., 2008), D. Wiemer for the DGBP inhibitor, Y. Wang for editing of the manuscript, M. Hendren for animal colony management, St. Jude Immunology flow cytometry core facility for cell

sorting, the Hartwell Center for microarray analysis, and Joshua Stokes of St. Jude Biomedical Communications for artwork. This work was supported by NIH grants NIH AI1055887, AI131703, AI140761, AI150241, AI150514, and CA221290 (to H.C.). The content is solely the responsibility of the authors and does not necessarily represent the official views of the National Institutes of Health.

References

Akula MK, Ibrahim MX, Ivarsson EG, Khan OM, Kumar IT, Erlandsson M, Karlsson C, Xu X, Brisslert M, Brakebusch C, et al. (2019). Protein prenylation restrains innate immunity by inhibiting Rac1 effector interactions. Nat Commun 10, 3975. [PubMed: 31484924]

Arvey A, van der Veeken J, Samstein RM, Feng Y, Stamatoyannopoulos JA, and Rudensky AY (2014). Inflammation-induced repression of chromatin bound by the transcription factor Foxp3 in regulatory T cells. Nat Immunol 15, 580–587. [PubMed: 24728351]

Bailey TL, Boden M, Buske FA, Frith M, Grant CE, Clementi L, Ren J, Li WW, and Noble WS (2009). MEME SUITE: tools for motif discovery and searching. Nucleic Acids Res 37, W202–208. [PubMed: 19458158]

Berndt N, Hamilton AD, and Sebti SM (2011). Targeting protein prenylation for cancer therapy. Nat Rev Cancer 11, 775–791. [PubMed: 22020205]

Buenrostro JD, Giresi PG, Zaba LC, Chang HY, and Greenleaf WJ (2013). Transposition of native chromatin for fast and sensitive epigenomic profiling of open chromatin, DNA-binding proteins and nucleosome position. Nat Methods 10, 1213–1218. [PubMed: 24097267]

Chapman NM, Zeng H, Nguyen TM, Wang Y, Vogel P, Dhungana Y, Liu X, Neale G, Locasale JW, and Chi H (2018). mTOR coordinates transcriptional programs and mitochondrial metabolism of activated Treg subsets to protect tissue homeostasis. Nat Commun 9, 2095. [PubMed: 29844370]

Cretney E, Xin A, Shi W, Minnich M, Masson F, Miasari M, Belz GT, Smyth GK, Busslinger M, Nutt SL, and Kallies A (2011). The transcription factors Blimp-1 and IRF4 jointly control the differentiation and function of effector regulatory T cells. Nat Immunol 12, 304–311. [PubMed: 21378976]

Du X, Zeng H, Liu S, Guy C, Dhungana Y, Neale G, Bergo MO, and Chi H (2020). Mevalonate metabolism-dependent protein geranylgeranylation regulates thymocyte egress. J Exp Med 217, e20190969. [PubMed: 31722972]

Galgani M, De Rosa V, La Cava A, and Matarese G (2016). Role of Metabolism in the Immunobiology of Regulatory T Cells. J Immunol 197, 2567–2575. [PubMed: 27638939]

Gusmao EG, Allhoff M, Zenke M, and Costa IG (2016). Analysis of computational footprinting methods for DNase sequencing experiments. Nat Methods 13, 303–309. [PubMed: 26901649]

Huynh A, DuPage M, Priyadharshini B, Sage PT, Quiros J, Borges CM, Townamchai N, Gerriets VA, Rathmell JC, Sharpe AH, et al. (2015). Control of PI(3) kinase in Treg cells maintains homeostasis and lineage stability. Nat Immunol 16, 188–196. [PubMed: 25559257]

Karmaus PWF, Chen X, Lim SA, Herrada AA, Nguyen TM, Xu B, Dhungana Y, Rankin S, Chen W, Rosencrance C, et al. (2019). Metabolic heterogeneity underlies reciprocal fates of TH17 cell stemness and plasticity. Nature 565, 101–105. [PubMed: 30568299]

Khan OM, Ibrahim MX, Jonsson IM, Karlsson C, Liu M, Sjogren AK, Olofsson FJ, Brisslert M, Andersson S, Ohlsson C, et al. (2011). Geranylgeranyltransferase type I (GGTase-I) deficiency hyperactivates macrophages and induces erosive arthritis in mice. J Clin Invest 121, 628–639. [PubMed: 21266780]

Kidani Y, Elsaesser H, Hock MB, Vergnes L, Williams KJ, Argus JP, Marbois BN, Komisopoulou E, Wilson EB, Osborne TF, et al. (2013). Sterol regulatory element-binding proteins are essential for the metabolic programming of effector T cells and adaptive immunity. Nat Immunol 14, 489–499. [PubMed: 23563690]

Koizumi SI, Sasaki D, Hsieh TH, Taira N, Arakaki N, Yamasaki S, Wang K, Sarkar S, Shirahata H, Miyagi M, and Ishikawa H (2018). JunB regulates homeostasis and suppressive functions of effector regulatory T cells. Nat Commun 9, 5344. [PubMed: 30559442]

Lacher SM, Bruttger J, Kalt B, Berthelet J, Rajalingam K, Wortge S, and Waisman A (2017). HMG-CoA reductase promotes protein prenylation and therefore is indispensible for T-cell survival. Cell Death Dis 8, e2824. [PubMed: 28542128]

Levine AG, Arvey A, Jin W, and Rudensky AY (2014). Continuous requirement for the TCR in regulatory T cell function. Nat Immunol 15, 1070–1078. [PubMed: 25263123]

Li H, and Durbin R (2009). Fast and accurate short read alignment with Burrows-Wheeler transform. Bioinformatics 25, 1754–1760. [PubMed: 19451168]

Li H, Handsaker B, Wysoker A, Fennell T, Ruan J, Homer N, Marth G, Abecasis G, Durbin R, and Genome Project Data Processing, S. (2009). The Sequence Alignment/Map format and SAMtools. Bioinformatics 25, 2078–2079. [PubMed: 19505943]

Li MO, and Rudensky AY (2016). T cell receptor signalling in the control of regulatory T cell differentiation and function. Nat Rev Immunol 16, 220–233. [PubMed: 27026074]

Li Z, Schulz MH, Look T, Begemann M, Zenke M, and Costa IG (2019). Identification of transcription factor binding sites using ATAC-seq. Genome Biol 20, 45. [PubMed: 30808370]

Liu M, Sjogren AK, Karlsson C, Ibrahim MX, Andersson KM, Olofsson FJ, Wahlstrom AM, Dalin M, Yu H, Chen Z, et al. (2010). Targeting the protein prenyltransferases efficiently reduces tumor development in mice with K-RAS-induced lung cancer. Proc Natl Acad Sci U S A 107, 6471–6476. [PubMed: 20308544]

Luo CT, Liao W, Dadi S, Toure A, and Li MO (2016). Graded Foxo1 activity in Treg cells differentiates tumour immunity from spontaneous autoimmunity. Nature 529, 532–536. [PubMed: 26789248]

Mullen PJ, Yu R, Longo J, Archer MC, and Penn LZ (2016). The interplay between cell signalling and the mevalonate pathway in cancer. Nat Rev Cancer 16, 718–731. [PubMed: 27562463]

Newton R, Priyadharshini B, and Turka LA (2016). Immunometabolism of regulatory T cells. Nat Immunol 17, 618–625. [PubMed: 27196520]

Oh H, Grinberg-Bleyer Y, Liao W, Maloney D, Wang P, Wu Z, Wang J, Bhatt DM, Heise N, Schmid RM, et al. (2017). An NF-kappaB Transcription-Factor-Dependent Lineage-Specific Transcriptional Program Promotes Regulatory T Cell Identity and Function. Immunity 47, 450–465 e455. [PubMed: 28889947]

Quinlan AR, and Hall IM (2010). BEDTools: a flexible suite of utilities for comparing genomic features. Bioinformatics 26, 841–842. [PubMed: 20110278]

Robinson JT, Thorvaldsdottir H, Winckler W, Guttman M, Lander ES, Getz G, and Mesirov JP (2011). Integrative genomics viewer. Nat Biotechnol 29, 24–26. [PubMed: 21221095]

Rubtsov YP, Rasmussen JP, Chi EY, Fontenot J, Castelli L, Ye X, Treuting P, Siewe L, Roers A, Henderson WR Jr., et al. (2008). Regulatory T cell-derived interleukin-10 limits inflammation at environmental interfaces. Immunity 28, 546–558. [PubMed: 18387831]

Savage PA, Klawon DEJ, and Miller CH (2020). Regulatory T Cell Development. Annu Rev Immunol 38, 421–453. [PubMed: 31990619]

Shi H, Liu C, Tan H, Li Y, Nguyen TM, Dhungana Y, Guy C, Vogel P, Neale G, Rankin S, et al. (2018). Hippo Kinases Mst1 and Mst2 Sense and Amplify IL-2R-STAT5 Signaling in Regulatory T Cells to Establish Stable Regulatory Activity. Immunity 49, 899–914 e896. [PubMed: 30413360]

Shrestha S, Yang K, Guy C, Vogel P, Neale G, and Chi H (2015). Treg cells require the phosphatase PTEN to restrain TH1 and TFH cell responses. Nat Immunol 16, 178–187. [PubMed: 25559258]

Smigiel KS, Richards E, Srivastava S, Thomas KR, Dudda JC, Klonowski KD, and Campbell DJ (2014). CCR7 provides localized access to IL-2 and defines homeostatically distinct regulatory T cell subsets. J Exp Med 211, 121–136. [PubMed: 24378538]

Sun IH, Oh MH, Zhao L, Patel CH, Arwood ML, Xu W, Tam AJ, Blosser RL, Wen J, and Powell JD (2018). mTOR Complex 1 Signaling Regulates the Generation and Function of Central and Effector Foxp3(+) Regulatory T Cells. J Immunol 201, 481–492. [PubMed: 29884702]

Tan H, Yang K, Li Y, Shaw TI, Wang Y, Blanco DB, Wang X, Cho JH, Wang H, Rankin S, et al. (2017). Integrative Proteomics and Phosphoproteomics Profiling Reveals Dynamic Signaling Networks and Bioenergetics Pathways Underlying T Cell Activation. Immunity 46, 488–503. [PubMed: 28285833]

Vasanthakumar A, Liao Y, Teh P, Pascutti MF, Oja AE, Garnham AL, Gloury R, Tempany JC, Sidwell T, Cuadrado E, et al. (2017). The TNF Receptor Superfamily-NF-kappaB Axis Is Critical to

Maintain Effector Regulatory T Cells in Lymphoid and Non-lymphoid Tissues. Cell Rep 20, 2906–2920. [PubMed: 28889989]

Vasanthakumar A, Moro K, Xin A, Liao Y, Gloury R, Kawamoto S, Fagarasan S, Mielke LA, Afshar-Sterle S, Masters SL, et al. (2015). The transcriptional regulators IRF4, BATF and IL-33 orchestrate development and maintenance of adipose tissue-resident regulatory T cells. Nat Immunol 16, 276–285. [PubMed: 25599561]

Wakamatsu E, Mathis D, and Benoist C (2013). Convergent and divergent effects of costimulatory molecules in conventional and regulatory CD4+ T cells. Proc Natl Acad Sci U S A 110, 1023–1028. [PubMed: 23277554]

Wang M, and Casey PJ (2016). Protein prenylation: unique fats make their mark on biology. Nat Rev Mol Cell Biol 17, 110–122. [PubMed: 26790532]

Wei J, Long L, Yang K, Guy C, Shrestha S, Chen Z, Wu C, Vogel P, Neale G, Green DR, and Chi H (2016). Autophagy enforces functional integrity of regulatory T cells by coupling environmental cues and metabolic homeostasis. Nat Immunol 17, 277–285. [PubMed: 26808230]

Wei J, Long L, Zheng W, Dhungana Y, Lim SA, Guy C, Wang Y, Wang YD, Qian C, Xu B, et al. (2019). Targeting REGNASE-1 programs long-lived effector T cells for cancer therapy. Nature 576, 471–476. [PubMed: 31827283]

Weinberg SE, Singer BD, Steinert EM, Martinez CA, Mehta MM, Martinez-Reyes I, Gao P, Helmin KA, Abdala-Valencia H, Sena LA, et al. (2019). Mitochondrial complex III is essential for suppressive function of regulatory T cells. Nature 565, 495–499. [PubMed: 30626970]

Whibley N, Tucci A, and Powrie F (2019). Regulatory T cell adaptation in the intestine and skin. Nat Immunol 20, 386–396. [PubMed: 30890797]

Yang K, Neale G, Green DR, He W, and Chi H (2011). The tumor suppressor Tsc1 enforces quiescence of naive T cells to promote immune homeostasis and function. Nat Immunol 12, 888–897. [PubMed: 21765414]

Yang K, Shrestha S, Zeng H, Karmaus PW, Neale G, Vogel P, Guertin DA, Lamb RF, and Chi H (2013). T cell exit from quiescence and differentiation into Th2 cells depend on Raptor-mTORC1-mediated metabolic reprogramming. Immunity 39, 1043–1056. [PubMed: 24315998]

Zeng H, Yang K, Cloer C, Neale G, Vogel P, and Chi H (2013). mTORC1 couples immune signals and metabolic programming to establish T(reg)-cell function. Nature 499, 485–490. [PubMed: 23812589]

Zhang B, and Horvath S (2005). A general framework for weighted gene co-expression network analysis. Stat Appl Genet Mol Biol 4, Article17. [PubMed: 16646834]

Zhang Y, Liu T, Meyer CA, Eeckhoute J, Johnson DS, Bernstein BE, Nusbaum C, Myers RM, Brown M, Li W, and Liu XS (2008). Model-based analysis of ChIP-Seq (MACS). Genome Biol 9, R137. [PubMed: 18798982]

Zheng Y, Chaudhry A, Kas A, deRoos P, Kim JM, Chu TT, Corcoran L, Treuting P, Klein U, and Rudensky AY (2009). Regulatory T-cell suppressor program co-opts transcription factor IRF4 to control T(H)2 responses. Nature 458, 351–356. [PubMed: 19182775]

Highlights

- Protein farnesylation and geranylgeranylation are critical for T_{reg}-cell function
- Posttranslational lipid modifications exert temporal effects on eT_{reg}-cell programs
- Fntb promotes eT_{reg}-cell maintenance via mTORC1 and ICOS
- Pggt1b tunes TCR and Rac signals for eT_{reg}-cell differentiation

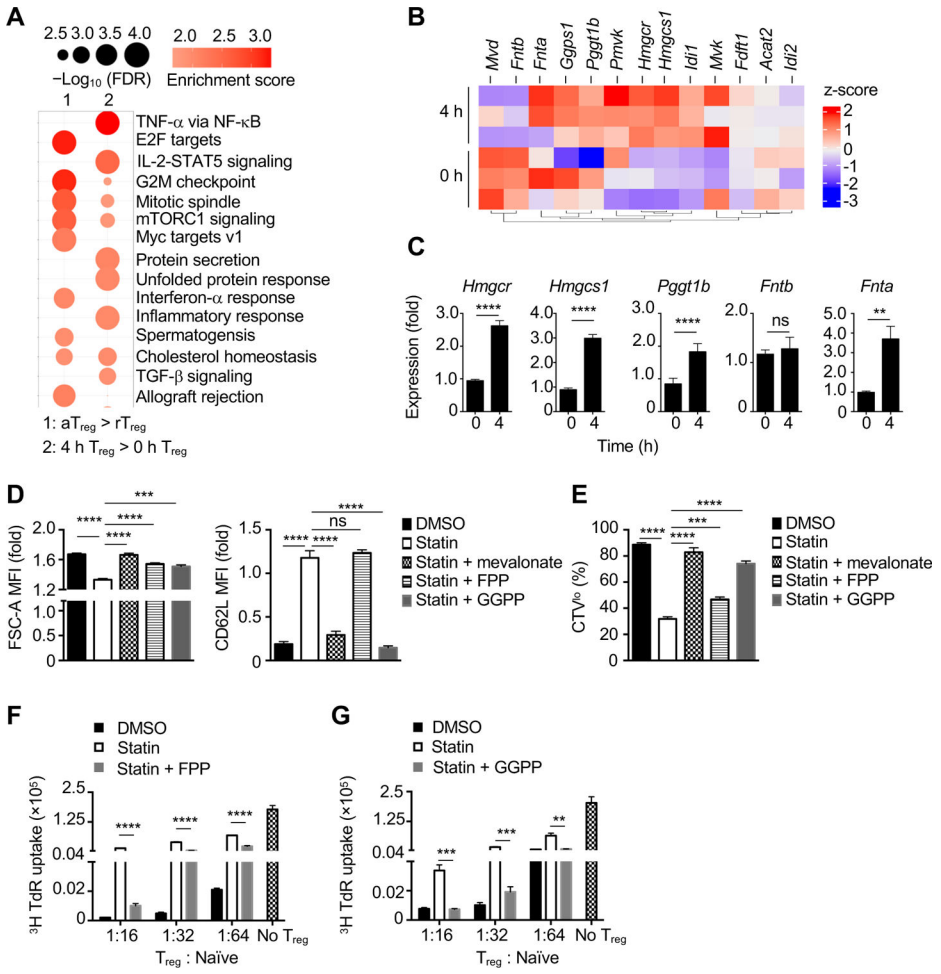

Figure 1. Mevalonate-derived isoprenoid synthesis is essential for suppressive activity of activated T_{reg} cells.

(A) Gene set enrichment analysis (GSEA) of the transcriptome of *in vivo* activated T_{reg} (aT_{reg}) compared to resting T_{reg} (rT_{reg}) cells (left) (Arvey et al., 2014), or T_{reg} cells stimulated with anti-CD3/28 for 0 or 4 h *in vitro* (right) (Wakamatsu et al., 2013). (B and C) Heat map (B) and real-time PCR analysis (C) of mevalonate pathway-related genes in T_{reg} cells activated for 0 or 4 h. (D and E) Quantification of cell size (FSC-A) (D), CD62L expression (D) and cell proliferation [Celltrace Violet (CTV^{lo})] (E) in aT_{reg} cells stimulated with anti-CD3/28 plus IL-2 for 3 days in the presence of DMSO or 2 μM simvastatin (statin) and supplied with indicated metabolites. MFI, mean fluorescence intensity. (F and G) aT_{reg} cells were generated as in (D and E) in the presence of 2 μM statin and supplied with 20 μM FPP or 5 μM GGPP, followed by co-culture with naïve $CD4^+$ T cells and assessment of aT_{reg}-cell suppressive activity.

Data are representative of two (F, G), or compiled from two (*Fnta* in C, D and E), four (*Hmgcr*, *Hmgcs1*, *Pggt1b*, *Fntb* in C) independent experiments, with at 4–6 (C) or 6 (D, E) biological replicates or 3 technical replicates (F, G) per group. *p < 0.05, **p < 0.01, ***p < 0.001, ****p < 0.0001, ns, not significant; two-tailed unpaired Student's *t*-test (C) or one-way ANOVA (D–G). Data are mean ± s.e.m. Fold change of 0 h (C) or IL-2 treatment (D). See also Figure S1.

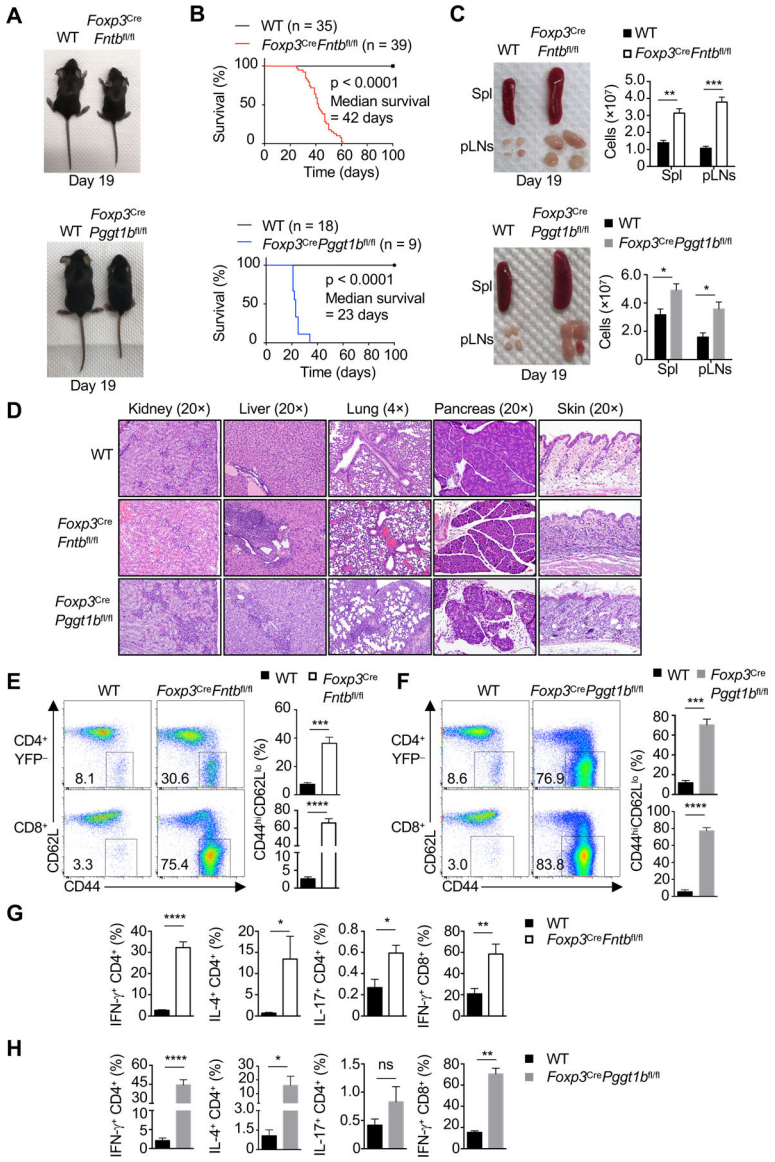

Figure 2. Fntb and Pggt1b in T_{reg} cells are indispensable for immune homeostasis.

(A) Representative images of 19-day-old *Foxp3*^{Cre}*Fntb*$^{fl/fl}$ mice or *Foxp3*^{Cre}*Pggt1b*$^{fl/fl}$ mice. (B) Survival of *Foxp3*^{Cre}*Fntb*$^{fl/fl}$ or *Foxp3*^{Cre}*Pggt1b*$^{fl/fl}$ mice. (C) Representative images and quantification of cell numbers of enlarged spleen (Spl) and peripheral lymph nodes (pLN) of mutant mice. (D) Representative H&E staining from indicated mice at 3 weeks. (E and F) Flow cytometry analysis of CD44^{hi}CD62L^{lo} CD4^{+}Foxp3-YFP^{-} or CD8^{+} T cells. Right, frequency of splenic CD44^{hi}CD62L^{lo} CD4^{+}Foxp3-YFP^{-} or CD8^{+} T cells. (G and H) Frequencies of splenic IFN-γ^{+}, IL-4^{+}, or IL-17^{+} CD4^{+} T cells and IFN-γ^{+} CD8^{+} T cells. Data are representative of seven (A, C, E, G) or one (D), or compiled from three (C, lower right; H) or two (F, G) independent experiments, with 3–4 (C, E–H) mice per group. *p < 0.05, **p < 0.01, ***p < 0.001, ****p < 0.0001, ns, not significant; two-tailed unpaired Student's *t*-test (C, E– H). Data are mean ± s.e.m. Numbers indicate percentage of cells in gates. See also Figure S2.

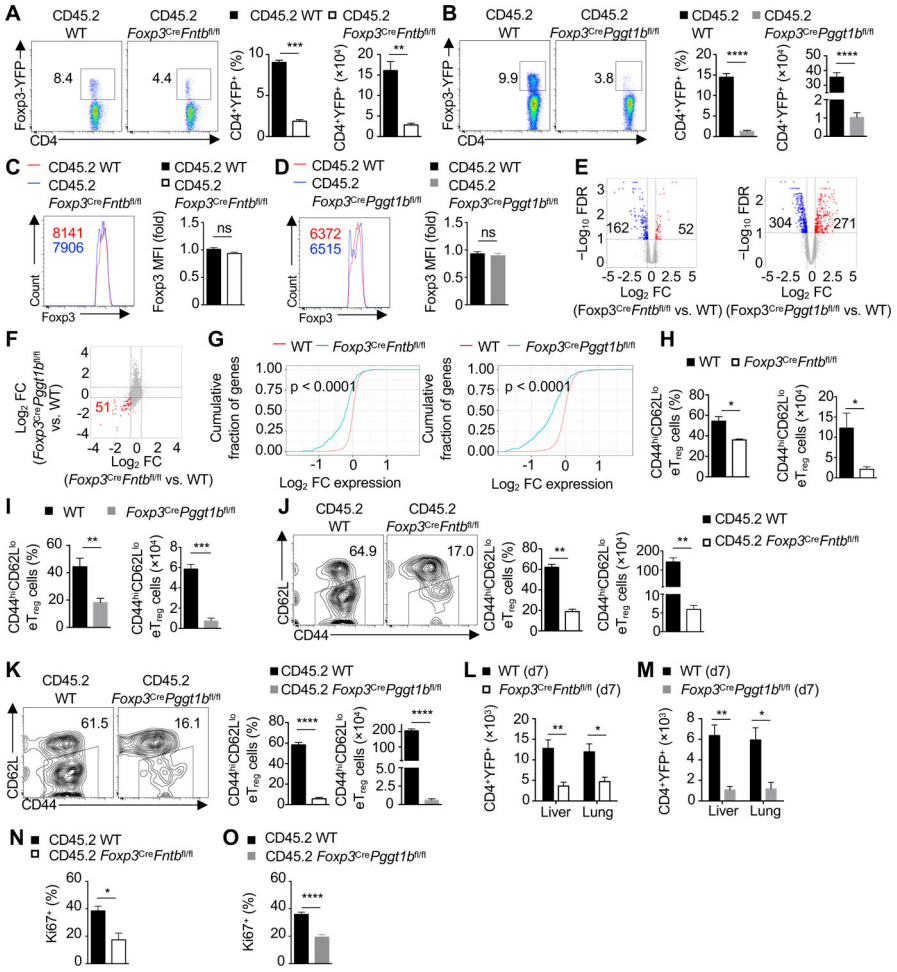

Figure 3. Crucial roles of Fntb and Pggt1b in eT$_{reg}$-cell accumulation.

(A and B) Flow cytometry analysis of splenic CD45.2^{+}CD4^{+}Foxp3-YFP^{+} T$_{reg}$ cells in WT and *Foxp3*^{Cre}*Fntb*$^{fl/fl}$ (A) or *Foxp3*^{Cre}*Pggt1b*$^{fl/fl}$ (B) mixed bone marrow chimeras. Quantification of the frequency and number of T$_{reg}$ cells. (C and D) Flow cytometry analysis and quantification of Foxp3 mean fluorescence intensity (MFI) in splenic T$_{reg}$ cells from indicated mixed bone marrow chimeras. (E) Transcriptomic analysis and volcano plots of Fntb-deficient vs. WT or Pggt1b-deficient vs. WT Foxp3-YFP^{+} T$_{reg}$ cells from mixed bone marrow chimeras. FDR, false discovery rate; FC, fold-change. (F) FC/FC plot of Pggt1b-deficient vs. WT T$_{reg}$ cells compared with Fntb-deficient vs. WT T$_{reg}$ cells as analyzed in (E). Number of shared downregulated genes is marked in red. (G) Cumulative distribution function plot of eT$_{reg}$-cell signature genes in Fntb-(left) or Pggtb1-deficient (right) T$_{reg}$ cells as compared with WT T$_{reg}$ cells. (H and I) Quantification of frequency (left) and number (right) of splenic CD44^{hi}CD62L^{lo} eT$_{reg}$ cells. (J and K) Flow cytometry analysis and quantification of splenic CD44^{hi}CD62L^{lo} eT$_{reg}$ cells in indicated mixed bone marrow chimeras. (L and M) Quantification of CD4^{+}YFP^{+} T$_{reg}$-cell number in the liver and lung from indicated neonatal mice at day 7 (d7). (N and O) Quantification of splenic Ki67^{+} T$_{reg}$ cell frequency from indicated mixed bone marrow chimeras.

Data are representative of four (J) or three (K), or compiled from two (A–D, I, N, O) or three (H) independent experiments, with 4–6 (A, C), 4–5 (B, D), 3–4 (H), 3 (I), 5 (L), 2 (J), 4 (K),

5 (M, O) or 6 (N) mice per group. *p < 0.05, **p < 0.01, ***p < 0.001, ****p < 0.0001, ns, not significant; two-tailed unpaired Student's *t*-test (A–D, H–O). Data are mean ± s.e.m. Numbers indicate percentage of cells in gates. See also Figure S3.

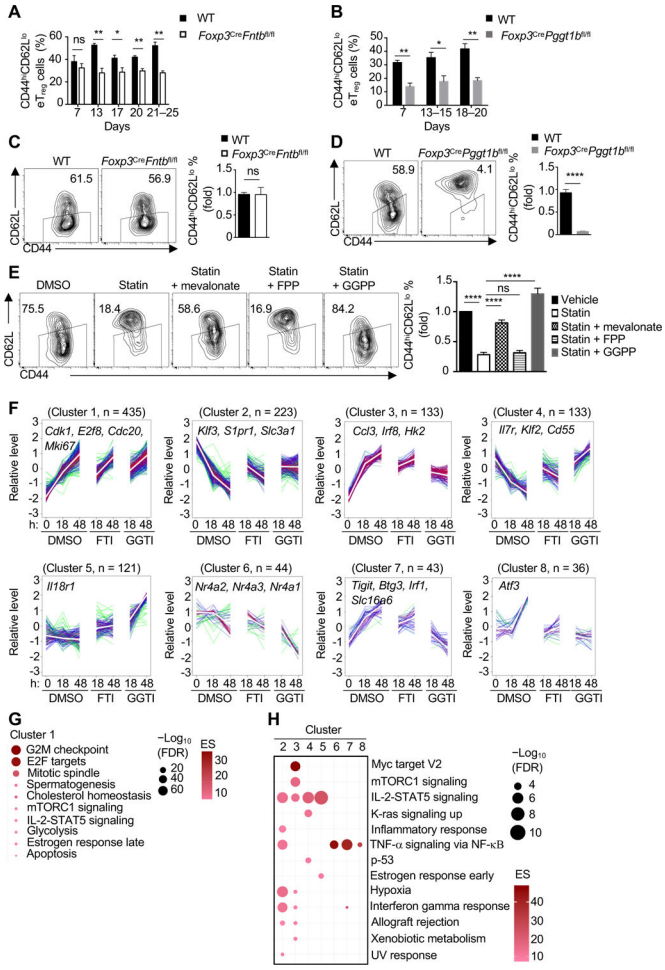

Figure 4. Fntb and Pggt1b orchestrate discrete transcriptional programming of eT$_{reg}$ cells.

(A and B) Quantification of CD44^{hi}CD62L^{lo} eT$_{reg}$-cell percentage in peripheral lymph nodes at the indicated ages. (C and D) Flow cytometry and quantification of eT$_{reg}$-like cells generated from cT$_{reg}$ cells isolated from the indicated mice. (E) cT$_{reg}$ cells were activated with anti-CD3/28 plus IL-2 for 3 days in the presence of DMSO or simvastatin (statin) with or without mevalonate, FPP or GGPP. Flow cytometry analysis and quantification of eT$_{reg}$-like cell generation. (F) Weighted gene correlation network analysis (WGCNA) of cT$_{reg}$ cells activated with anti-CD3/28 plus IL-2 for the indicated times in the presence of DMSO, FTI, or GGTI. The number of genes in each cluster, and representative gene names, are indicated. (G and H) Functional enrichment of hallmark pathways in cluster 1 (G) or clusters 2–8 (H) from WGCNA.

Data are compiled from three (A for day 7 and days 21–25, B for day 7 and days 13–15, D), two (A for day 17, B for days 18–20, E), one (A for day 13 and day 20) or five (C) independent experiments, with at least 3–5 (A), 3–6 (B), 5 (C), 4 (D) or 6 (E) biological replicates per group. *p < 0.05, **p < 0.01, ****p < 0.0001, ns, not significant; two-tailed unpaired Student's *t*-test (A–D) or one-way ANOVA (E). Data are mean ± s.e.m. Controls were normalized to 1 for each comparison (black bars) (C–E). See also Figure S4.

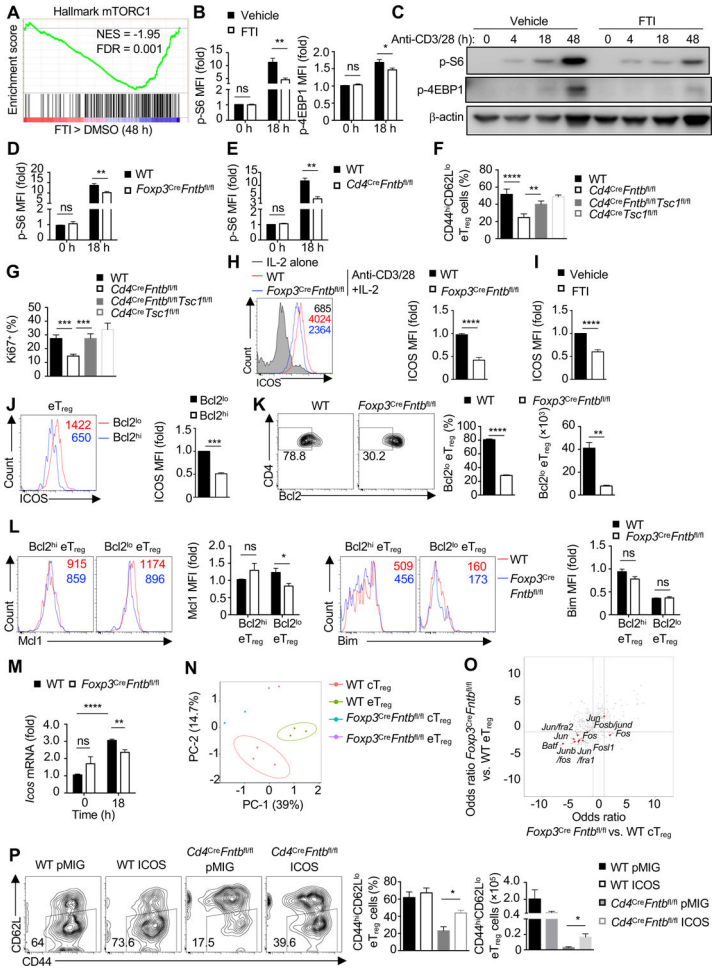

Figure 5. Fntb promotes the maintenance of eT$_{reg}$ cells by mTORC1 and ICOS signaling.

(A) Gene set enrichment analysis (GSEA) of the hallmark mTORC1 pathway in cT$_{reg}$ cells stimulated with anti-CD3/28 plus IL-2 in the presence of vehicle or FTI for 48 h. (B) Quantification of the relative mean fluorescence intensity (MFI) of phosphorylated S6 (p-S6) and p-4EBP1 by flow cytometry analysis in WT cT$_{reg}$ cells stimulated with anti-CD3/28 plus IL-2 in the presence of FTI for 0 or 18 h. (C) Immunoblot analysis of p-S6 and p-4EBP1 in cT$_{reg}$ cells stimulated as in (B) for the indicated times. (D) Quantification of relative MFI of p-S6 in cT$_{reg}$ cells from WT or *Foxp3*^{Cre}*Fntb*$^{fl/fl}$ mice stimulated as in (B). (E) Quantification of relative MFI of p-S6 in cT$_{reg}$ cells from WT and *Cd4*^{Cre}*Fntb*$^{fl/fl}$ mice stimulated as in (B). (F and G) Quantification of percentage of splenic CD44^{hi}CD62L^{lo} eT$_{reg}$ cells (F) or Ki67^{+} T$_{reg}$ cells percentage in WT, *Cd4*^{Cre}*Fntb*$^{fl/fl}$, *Cd4*^{Cre}*Fntb*$^{fl/fl}$*Tsc1*$^{fl/fl}$ or *Cd4*^{Cre}*Tsc1*$^{fl/fl}$ mice. (H) Flow cytometry analysis and quantification of ICOS expression on cT$_{reg}$ cells isolated from indicated mice after IL-2 or anti-CD3/28 plus IL-2 stimulation for 3 days. (I) Quantification of ICOS expression on WT cT$_{reg}$ cells stimulated as in (H) in the presence of vehicle or FTI. (J) Flow cytometry analysis and quantification of ICOS expression on WT Bcl2^{lo} and Bcl2^{hi} eT$_{reg}$-cell subsets from spleen. (K) Flow cytometry analysis (left) and quantification of frequency (middle) and number (right) of splenic Bcl2^{lo} eT$_{reg}$ cells in indicated mice. (L) Flow cytometry analysis and quantification of Mcl1 (left) or Bim (right) expression (based on mean fluorescence intensity, MFI) in splenic Bcl2^{hi} and

$Bcl2^{lo}$ eT_{reg} cells from indicated mice. (M) *Icos* expression in cT_{reg} cells from indicated mice after stimulation as in (B). (N) Principal component analysis plot of nucleosome-free reads of cT_{reg} and eT_{reg} cells from WT or $Foxp3^{Cre}Fntb^{fl/fl}$ mixed bone marrow chimeras. (O) Odds ratio/odds ratio plot of the predicted enriched motifs in $Foxp3^{Cre}Fntb^{fl/fl}$ vs. WT eT_{reg} cells compared with $Foxp3^{Cre}Fntb^{fl/fl}$ vs. WT cT_{reg} from mixed bone marrow chimeras. (P) Flow cytometry and quantification of splenic eT_{reg} cell percentage and number in retrogenic mice [WT or $Cd4^{Cre}Fntb^{fl/fl}$ bone marrow cells were transduced with pMIG-GFP empty vector (pMIG) or pMIG-GFP-ICOS (ICOS) retroviral vector; see Methods]. Data are representative of two (C) or four (J, K), or compiled from two (B for p-4EBP1, L for Bim, M), three (B for p-S6, D, E, L for Mcl1, P), four (F, G, J, K), five (H) or six (I) independent experiments, with 9 (B for p-S6), 7 (L for Mcl1), 6 (B for p-4EBP1, I, L for Bim, P for WT pMIG and WT ICOS), 3 (E, M, P for $Cd4^{Cre}Fntb^{fl/fl}$ pMIG), 4 (F, G, J, K, P for $Cd4^{Cre}Fntb^{fl/fl}$ ICOS) or 5 (D, H) biological replicates per group. *$p < 0.05$, **$p < 0.01$, ***$p < 0.001$, ****$p < 0.0001$, ns, not significant; two-tailed unpaired Student's *t*-test (B, D, E, H–K, L–P) or one-way ANOVA (F, G). Data are mean ± s.e.m. Numbers indicate percentage of cells in gates. Numbers in histograms indicate MFI. Controls were normalized to 1 for each comparison (usually in black bars). See also Figure S5.

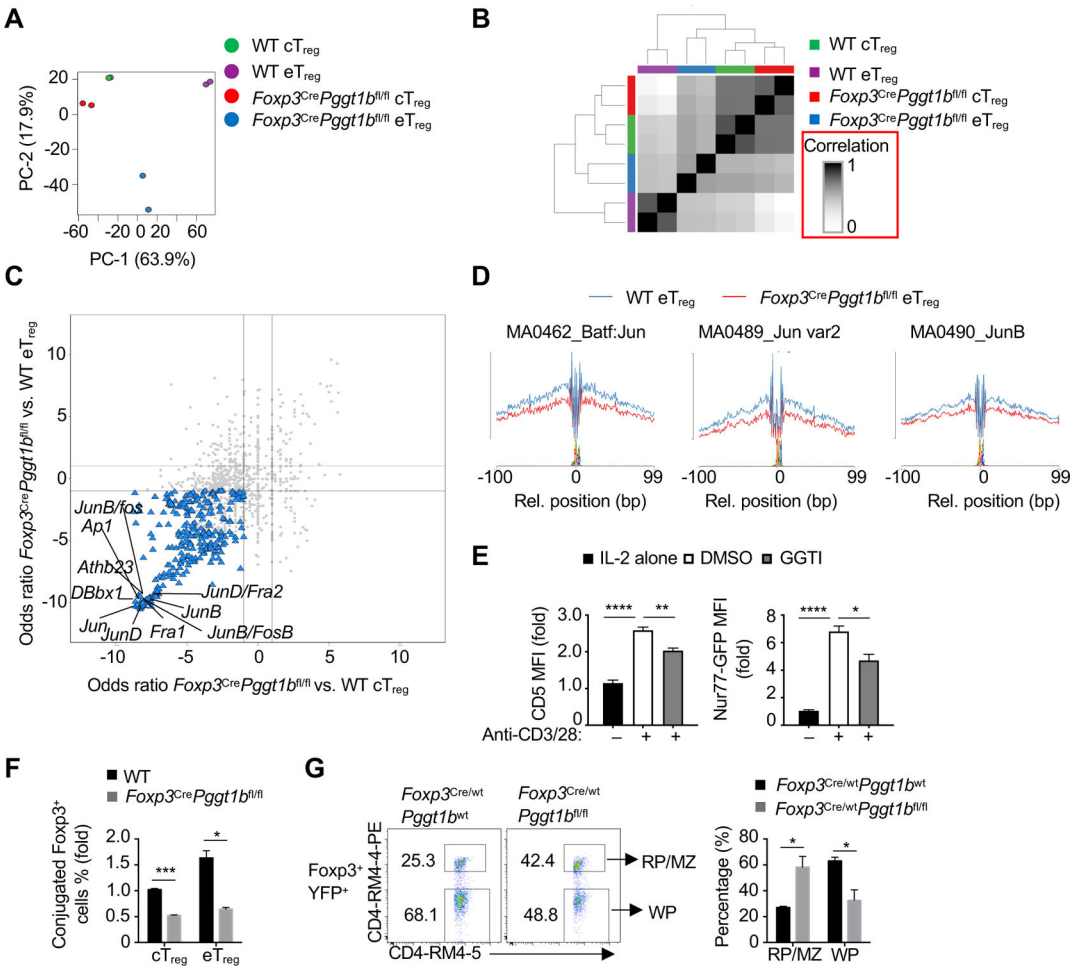

Figure 6. Pggt1b shapes chromatin accessibility and AP-1 transcriptional programming.

(A) Principal component analysis plot of nucleosome-free reads of cT_{reg} and eT_{reg} cells from WT or *Foxp3*^{Cre}*Pggt1b*$^{fl/fl}$ mixed bone marrow chimeras. (B) Similarity matrix plot of indicated cell populations as in (A). (C) Odds ratio/odds ratio plot of the predicted enriched motifs in *Foxp3*^{Cre}*Pggt1b*$^{fl/fl}$ vs. WT eT_{reg} cells compared with *Foxp3*^{Cre}*Pggt1b*$^{fl/fl}$ vs. WT cT_{reg} as in (A). (D) Binding profiles of Jun family transcription factors in WT or *Foxp3*^{Cre}*Pggt1b*$^{fl/fl}$ eT_{reg} cells as in (A). (E) Quantification of CD5 or Nur77-GFP expression in Foxp3-RFP^{+} cT_{reg} cells activated by anti-CD3/28 plus IL-2 (or IL-2 alone, black bars) in the presence or absence of GGTI for 24 h. (F) Quantification of conjugate formation of Foxp3-YFP^{+} cT_{reg} or eT_{reg} cells from WT or *Foxp3*^{Cre}*Pggt1b*$^{fl/fl}$ mice co-cultured with Celltrace Violet-labeled DCs in the presence of IL-2 for 10 h. (G) Flow cytometry analysis and quantification of the frequency of Foxp3^{+}YFP^{+} T_{reg} cells from WT or *Foxp3*$^{Cre/wt}$*Pggt1b*$^{fl/fl}$ 'mosaic' mice found in the red pulp/marginal zone(RP/MZ; CD4-RM4–5^{+}CD4-RM4–4-PE^{+}) or white pulp (WP; CD4-RM4–5^{+}CD4-RM4–4-PE^{-}).

Data are representative of two (E), or compiled from two (F, G) independent experiments, with three (E, G) or at least two (F) biological replicates per group. *p < 0.05, **p < 0.01, ***p < 0.001, ****p < 0.0001; two-tailed unpaired Student's *t*-test (F, G) or one-way ANOVA (E). Data are mean ± s.e.m. Numbers indicate percentage of cells in gates. Controls were normalized to 1 for each comparison (black bars). See also Figure S6.

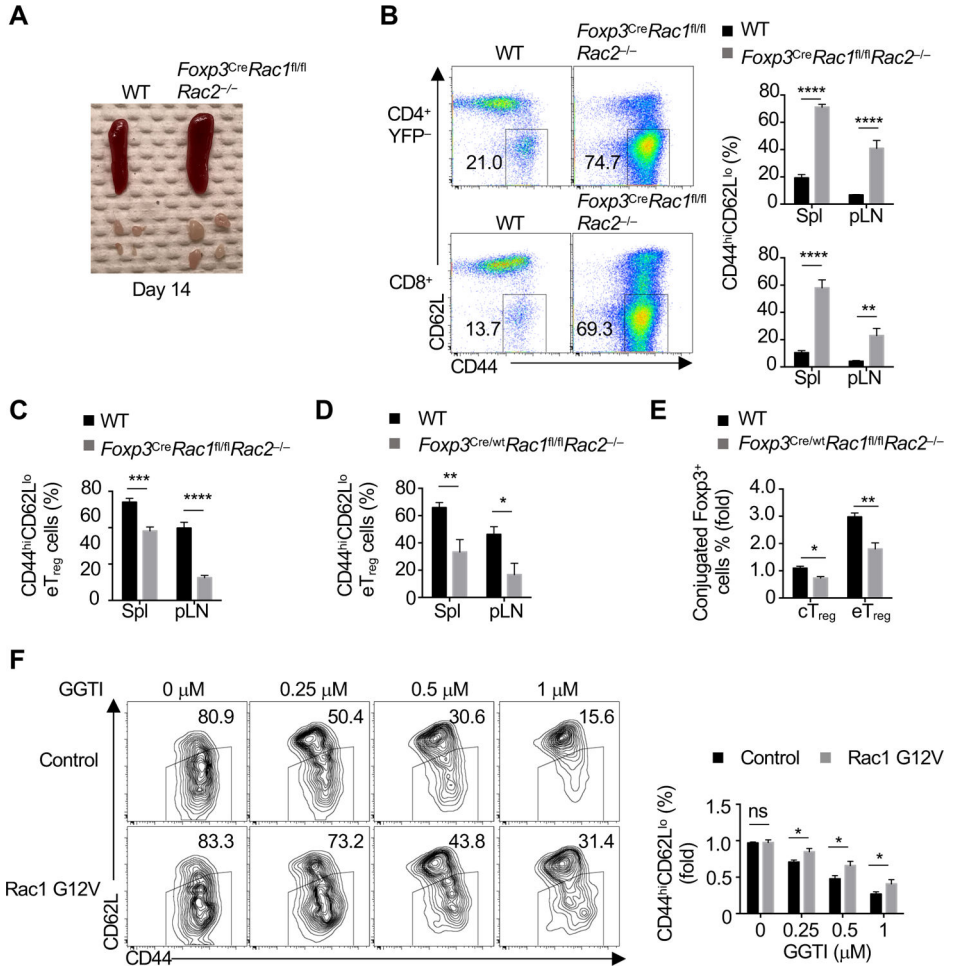

Figure 7. Rac is essential for eT$_{reg}$-cell differentiation and immune homeostasis.

(A) Representative images of enlarged spleen and peripheral lymph nodes (pLN) in WT and *Foxp3*^{Cre}*Rac1*$^{fl/fl}$*Rac2*$^{-/-}$ mice. (B) Flow cytometry analysis (spleen) and quantification of the frequency of CD44^{hi}CD62L^{lo} CD4^{+}Foxp3-YFP^{-} or CD8^{+} T cells in the spleen (Spl) and pLN of indicated mice. (C) Quantification of the frequency of CD4^{+}Foxp3-YFP^{+} eT$_{reg}$ cells in the Spleen and pLN of WT and *Foxp3*^{Cre}*Rac1*$^{fl/fl}$*Rac2*$^{-/-}$ mice. (D) Quantification of eT$_{reg}$ cell frequency in indicated organs of WT and *Foxp3*$^{Cre/wt}$*Rac1*$^{fl/fl}$*Rac2* $^{-/-}$ 'mosaic' mice. (E) Quantification of conjugate formation of Foxp3-YFP^{+} cT$_{reg}$ or eT$_{reg}$ cells from indicated 'mosaic' mice co-cultured with Celltrace Violet (CTV)-labeled DCs after co-culture in the presence of IL-2 for 10 h. (F) WT cT$_{reg}$ cells activated by anti-CD3/28 for 18 h were transduced with retrovirus expressing empty vector control or Rac1 G12V vector. After resting, CTV-labeled transduced cells pretreated with the indicated doses of GGTI for 2 h were activated with anti-CD3/28 plus IL-2 for 3 days. Flow cytometry analysis and quantification of eT$_{reg}$-like cell generation.

Data are representative of three (A), or compiled from three (B and C), two (D-E) or three (F) independent experiments, with 7–8 (B, C), 3–5 (D, E) or 10–11 (F) biological replicates per group. *p < 0.05, **p < 0.01, ***p < 0.001, ****p < 0.0001; ns, not significant; two-tailed unpaired Student's *t*-test (B–F). Data are mean ± s.e.m. Numbers indicate percentage

of cells in gates. Controls were normalized to 1 for each comparison (black bars). See also Figure S7.

KEY RESOURCES TABLE

REAGENT or RESOURCE	SOURCE	IDENTIFIER
Antibodies		
Anti-CD4 (RM4–5)	Thermo Fisher Scientific	Cat# 48–0042-80; RRID:AB_1272231
Anti-CD4 (RM4–4, *in vivo* labeling)	BioLegend	Cat# 116006; RRID:AB_313691
Anti-CD8α (53–6.7)	BioLegend	Cat# 100742; RRID:AB_2563056
Anti-TCRβ (H57–597)	Thermo Fisher Scientific	Cat# 47–5961-82; RRID:AB_1272173
Anti-CD44 (1M7)	BioLegend	Cat# 103047; RRID:AB_2562451
Anti-CD62L (MEL-14)	Tonbo Biosciences	Cat# 60–0621; RRID:AB_469632
Anti-CD69 (H1.2F3)	Thermo Fisher Scientific	Cat# 48–0691-82; RRID:AB_10719430
Anti-PD-1 (J43)	Thermo Fisher Scientific	Cat# 17–9985-80; RRID:AB_11149860
Anti-CD45.1 (A20)	BioLegend	Cat# 110736; RRID:AB_2562564
Anti-CD45.2 (104)	Thermo Fisher Scientific	Cat# 48–0454-80; RRID:AB_11039533
Anti-CD25 (PC61.5)	Thermo Fisher Scientific	Cat# 17–0251-82; RRID:AB_469366
Anti-Foxp3 (FJK-16s)	Thermo Fisher Scientific	Cat# 12–5773-80; RRID:AB_465935
Anti-Ki67 (SolA15)	Thermo Fisher Scientific	Cat# 25–5698-80; RRID:AB_11217689
Anti-Bim (C34C5)	Cell Signaling Technology	Cat# 2933; RRID:AB_1030947
Anti-GFP-Alexa Fluor 488 (FM264G)	BioLegend	Cat# 338008; RRID:AB_2563288
Anti-IFN-γ (XMG1.2)	Thermo Fisher Scientific	Cat# 17–7311-81; RRID:AB_469503
Anti-IL-4 (11B11)	Thermo Fisher Scientific	Cat# 12–7041-71; RRID:AB_466154
Anti-IL-17 (eBio17B7)	Thermo Fisher Scientific	Cat# 45–7177-80; RRID:AB_925754
Anti-CD3 (145–2C11)	Bio-X-Cell	Cat# BE0001; RRID:AB_2714218
Anti-CD28 (37.51)	Bio-X-Cell	Cat# BE0015–1; RRID:AB_1107624
Anti-β-actin (C4)-HRP	Santa Cruz Biotechnology	Cat# sc-47778 HRP; AB_2714189
Anti-β-tubulin	Cell Signaling Technology	Cat# 2146, RRID:AB_2210545
Anti-phospho-S6 (S235/236) (D57.2.2E)	Cell Signaling Technology	Cat# 4858; RRID:AB_916156
Anti-phospho-4EBP1 (Thr37/46) (236B4)	Cell Signaling Technology	Cat# 2855; RRID: AB_560835
Anti-phospho-4EBP1 (Thr37/46) (236B4) -Alexa Fluor 647 conjugate	Cell Signaling Technology	Cat# 5123 RRID: AB_2097838
Anti-phospho-S6 (S235/236) (D57.2.2E)-Pacific Blue™ conjugate	Cell Signaling Technology	Cat# 8520, RRID:AB_2797646
Anti-Mcl1 (LVUBKM)	Thermo Fisher Scientific	Cat# 12–9047-42, RRID:AB_2762598
Anti-Bcl2 (BCL/10C4)	BioLegend	Cat# 633510, RRID:AB_2274702

REAGENT or RESOURCE	SOURCE	IDENTIFIER
Anti-ICOS (7E.17G9)	Thermo Fisher Scientific	Cat# 12–9942-82, RRID:AB_466274
Anti-CTLA4 (UC10–4B9)	BioLegend	Cat# 106312, RRID:AB_2563063
Anti-KLRG1 (2F1)	BioLegend	Cat# 138419, RRID:AB_2563357
Anti-CXCR3 (CXCR3–173)	BioLegend	Cat# 126531, RRID:AB_2563160
Anti-CD73 (TY/11.8)	BioLegend	Cat# 127212, RRID:AB_11219190
Anti-CD5 (53–7.3)	Thermo Fisher Scientific	Cat# 12–0051-81, RRID:AB_465522
Anti-Bim (C34C5)	Cell Signaling Technology	Cat# 12186, RRID:AB_2797842
Anti-Rap1A (C-17)	Santa Cruz Biotechnology	Cat# sc-1482, RRID:AB_2177124
Anti-HDJ2 (KA2A5.6)	Lab Vision	Cat# MS-225-P0, RRID:AB_61951
Anti-Rabbit IgG HRP conjugate	Promega	Cat# W4011, RRID:AB_430833
Anti-Mouse IgG HRP conjugate	Promega	Cat# W4021, RRID:AB_430834
Anti-Goat IgG HRP conjugate (sc-2345)	Santa Cruz Biotechnology	Cat# sc-2354, RRID:AB_628490
Chemicals, Peptides, and Recombinant Proteins		
7-Aminoactinoymycin D (7AAD)	Sigma-Aldrich	Cat# A9400
Simvastatin	Selleck Chemicals	Cat# S1792
FTI-277	Tocris	Cat# 2407
GGTI-2147	Sigma-Aldrich	Cat# 191102–87-1
(+)-Mevalonolactone (dehydrated mevalonate)	Sigma-Aldrich	Cat# M4667–5G
Farnesyl pyrophosphate ammonium salt (FPP)	Sigma-Aldrich	Cat# 13058–04-3
Geranylgeranyl pyrophosphate ammonium salt (GGPP)	Sigma-Aldrich	Cat# G6025
Fixable Viability Dye eFluor™ 780	Thermo Fisher Scientific	Cat# 65–0865-18
Recombinant human IL-2 (*in vitro* stimulation)	R&D Systems	Cat# 202-IL
Phobol 12-myristate 13-acetate (PMA)	Sigma-Aldrich	Cat# P8139
Ionomycin	Sigma-Aldrich	Cat# I0634
Golgi-STOP	BD Biosciences	Cat# 554724
Recombinant human IL-6	National Cancer Institute	Cat# NSC720836
Recombinant murine IL-3	Thermo Fisher Scientific	Cat# PMC0034
Recombinant murine stem-cell factor (SCF)	Thermo Fisher Scientific	Cat# PMC2115
ABI probe: *Pggt1b*	Thermo Fisher Scientific	Mm01266356_m1
ABI probe: *Icos*	Thermo Fisher Scientific	Mm00497600_m1
ABI probe: *Actb*	Thermo Fisher Scientific	Mm00607939_s1
Commercial Reagents		
Foxp3 transcription factor staining buffer set	Thermo Fisher Scientific	Cat# 00–5523-00
Cytofix/Cytoperm™ Fixation/Permeabilization Solution Kit	BD Biosciences	Cat# 554714
CD4 (3LT4) Microbeads, mouse	Miltenyi Biotec	Cat# 130–117-043
Lineage cell depletion kit	Miltenyi Biotec	Cat# 130–090-858
Transfection reagent	Mirus	Cat# MIR2706
10× Perm/Wash Buffer	BD Biosciences	Cat# 554723

REAGENT or RESOURCE	SOURCE	IDENTIFIER
Clariom S mouse array	Thermo Fisher Scientific	Cat# 902930
BD Phosflow™ Fix Buffer I	BD Biosciences	Cat# 557870
Phosflow™ Perm Buffer III	BD Biosciences	Cat# 558050
CellTrace™ Violet Cell Proliferation Kit	Thermo Fisher Scientific	Ca# C34557
Deposited Data		
Fntb- or Pggt1b-deficient T_{reg}-cell microarray data from mixed bone marrow chimeras	GEO (http://www.ncbi.nlm.nih.gov/geo/)	GSE158863
In vitro cT_{reg}-cell microarray data from DMSO, FTI, or GGTI treatments	GEO (http://www.ncbi.nlm.nih.gov/geo/)	GSE158863
ATAC-Seq data	GEO (http://www.ncbi.nlm.nih.gov/geo/)	GSE158863
Experimental Models: Cell Lines		
Plat-E	Dr. Yun-Cai Liu, La Jolla Institute of Immunology	N/A
Experimental Models: Organisms/Strains		
Mouse: C57BL/6J	The Jackson Laboratory	Cat# 000664; RRID:IMSR_JAX:000664
Mouse: *Fntb*$^{fl/fl}$	M. Bergo (Liu et al., 2010)	N/A
Mouse: *Pggt1b*$^{fl/fl}$	M. Bergo (Khan et al., 2011)	N/A
Mouse: *Hmgcr*$^{fl/fl}$	A. Waisman	N/A
Mouse: CD45.1^{+}: B6.SJL-*Ptprc*^{a} *Pepc*^{b}/BoyJ	The Jackson Laboratory	Cat# 002014; RRID:IMSR_JAX:002014
Mouse: *Cd4*^{Cre}: Tg(Cd4-cre)1Cwi/BfluJ	The Jackson Laboratory	Cat# 017336; RRID:IMSR_JAX:017336
Mouse: *Rag1*$^{-/-}$: *Rag1*^{tm1Mom}/J	The Jackson Laboratory	Cat# 002216; RRID:IMSR_JAX:002216
Mouse: Foxp3$^{YFP\text{-}Cre}$	A. Rudensky (Rubtsov et al., 2008)	N/A
Mouse: *Rac1*$^{fl/fl}$	The Jackson Laboratory	Cat# JAX:005550, RRID:IMSR_JAX:005550
Mouse: *Rac2*$^{-/-}$	The Jackson Laboratory	Cat# JAX:004197, RRID:IMSR_JAX:004197
Mouse: *Tsc1*$^{-/-}$	The Jackson Laboratory	Cat# JAX:005680, RRID:IMSR_JAX:005680
Mouse: C57BL/6-Tg(Nr4a1-EGFP/cre)820Khog/J (also known as Nur77-GFP)	The Jackson Laboratory	Cat# JAX:016617, RRID:IMSR_JAX:016617
Mouse: C57BL/6-*Foxp3*^{tm1Flv}/J (also known as Foxp3-RFP)	The Jackson Laboratory	Cat# JAX: 008374 RRID:IMSR JAX: 008374
Oligonucleotides		
Fntb-F: 5'-AACCGCTGTATAGTCTGAGACC-3'	This paper	N/A
Fntb-R: 5'-TCTCCCTCTGCAAAATGAGCC-3'	This paper	N/A
Hmgcr-F: 5'-AGCTTGCCCGAATTGTATGTG-3'	(Zeng et al., 2013)	N/A
Hmgcr-R: 5'-TCTGTTGTGAACCATGTGACTTC-3'	(Zeng et al., 2013)	N/A
Hmgcs1-F: 5'-AACTGGTGCAGAAATCTCTAGC-3'	(Zeng et al., 2013)	N/A
Hmgcs1-R: 5'-GGTTGAATAGCTCAGAACTAGCC-3'	(Zeng et al., 2013)	N/A
Fnta-F: 5'- CCCTATGGACGACGGGTTTC-3'	This paper	N/A

REAGENT or RESOURCE	SOURCE	IDENTIFIER
Fnta-R:5'- TGATCTGGACCACTGGGTTAG-3'	This paper	N/A
Actb-F: 5'-GACAGGATGCAGAAGGAGATTACTG-3'	This paper	N/A
Actb-R: 5'-GCTGATCCACATCTGCTGGAA-3'	This paper	N/A
Recombinant DNA		
pCAG4-Eco	Addgene	Addgene plasmid # 12260
pMX-GFP-Rac-G12V	(Shi et al., 2018)	Addgene Cat# 14567
ICOS cDNA ORF Clone	Sino Biological	MG50466-M
Software and Algorithms		
FlowJo v9.3	FlowJo	https://www.flowjo.com/
GraphPad Prism v6.0	GraphPad	https://www.graphpad.com/scientific-software/prism/
Other		
LSR Fortessa flow cytometer	BD Biosciences	N/A
MoFlow cell sorter	Beckman-Coulter	N/A
Reflection cell sorter	iCyt	N/A
ODYSSEY Fc Analyzer	LI-COR	N/A
Gene set enrichment analysis (GSEA) software suite	(Subramanian et al., 2005)	http://www.broadinstitute.org/gsea/msigdb/